AUGMENTED CLOTH FITTING WITH REAL TIME PHYSICS SIMULATION USING TIME-OF-FLIGHT CAMERAS

A THESIS

SUBMITTED TO THE DEPARTMENT OF COMPUTER ENGINEERING

AND THE GRADUATE SCHOOL OF ENGINEERING AND SCIENCE

OF BİLKENT UNIVERSITY

IN PARTIAL FULFILLMENT OF THE REQUIREMENTS

FOR THE DEGREE OF

MASTER OF SCIENCE

By

Umut Gültepe

December, 2012

I certify that I have read this thesis and that in my opinion it is fully adequate, in scope and in quality, as a thesis for the degree of Master of Science.

Assoc. Prof. Dr. Uğur Güdükbay (Supervisor)

I certify that I have read this thesis and that in my opinion it is fully adequate, in scope and in quality, as a thesis for the degree of Master of Science.

(Co-supervisor)

I certify that I have read this thesis and that in my opinion it is fully adequate, in scope and in quality, as a thesis for the degree of Master of Science.

I certify that I have read this thesis and that in my opinion it is fully adequate, in scope and in quality, as a thesis for the degree of Master of Science.

Approved for the Graduate School of Engineering and Science:

Prof. Dr. Levent Onural
Director of the Graduate School

ABSTRACT

AUGMENTED CLOTH FITTING WITH REAL TIME PHYSICS SIMULATION USING TIME-OF-FLIGHT CAMERAS

Umut Gültepe

M.S. in Computer Engineering

Supervisors: Assoc. Prof. Dr. Uğur Güdükbay

December, 2012

This study surveys and proposes a method for an augmented cloth fitting with real time physics simulation. Augmented reality is an evolving field in computer science, finding many uses in entertainment and advertising. With the advances in cloth simulation and time-of-flight cameras, augmented cloth fitting in real-time is developed , to be used in textile industry in both design and sale stages. Delay in cloth fitting due to processing time is the main challenge in this research. Human body is identified, articulated and tracked with a time-of-flight camera. Depending on the size and position of body limbs, a virtually simulated cloth is fitted in real time on the subject. Delay is reduced with GPU computing for cloth simulation and collision detection.

Keywords: cloth simluation, computer vision, natural interaction, virtual fitting room, kinect, depth sensor.

ÖZET

UÇUŞ ZAMANI KAMERALARI KULLANAN GERÇEK ZAMANLI FİZİK SİMÜLASYONLU ARTIRILMIŞ KIYAFET KABİNİ

Umut Gültepe
Bilgisayar Mühendisliği, Yüksek Lisans
Tez Yöneticileri: Doç. Dr. Uğur Güdükbay

Aralık, 2012

Bu çalışma fizik simülasyonlu bir artırılmış kıyafet giydirme için bir metot önermekte ve incelemektedir. Artırılmış gerçeklik bilgisayar biliminde gelişen bir alandır, eğlence ve reklam sektörlerinde geniş yer bulmaktadırlar. Kumaş simülasyonu ve uçuş-zamanı kameralarının geliştirilmesi ile, gerçek zamanlı artırılmış kıyafet giydirimi tekstil endüstrisinde tasarım ve satış aşamalarında kullanılmak üzere geliştirilmiştir. şleme zamanı sebebiyle kıyafet giydirilmesindeki gecikme bu araştırmadaki en büyük zorluktur. nsan vücudu bir uçuş-zamanı kamerası ile tanımlanmakta, bölünmekte ve takip edilmektedir. Vücut parçalarının boyutlarına ve pozisyonlarına göre simüle edilen bir sanal kıyafet kullanıcının üstüne yerleştirilmektedir. Gecikme zamanı kıyafet simülasyonunu ve çarpışma takibini GPU üzerinde yaparak azaltılmaktadır.

Anahtar sözcükler: kıyafet simülasyonu, bilgisayarla görü, doğal etkileşim, sanal giyinme kabini, kinect, derinlik sensörü.

Acknowledgement

I am deeply grateful to my supervisor Assoc. Prof. Dr. Uğur Güdükbay, who guided and assisted me with his invaluable suggestions in all stages of this study. I also chose this area of study by inspiring from his deep knowledge over this subject.

I am very grateful to Computer Engineering Department of Bilkent University for providing me scholarship for my MS study.

I would like to thank Scientific and Technical Research Council of Turkey (TÜBİTAK) and the Turkish Ministry of Industry and Technology for their financial support for this study and MS thesis.

to my mother, father and my brother...

Contents

List of Figures

List of Tables

List of Algorithms

Chapter 1

Introduction

A mesh is a collection of polygonal facets targeting to constitute an appropriate approximation of a real 3D object [1]. It has vertices, edges and facets. A mesh stores two kinds of information: *geometry* and *connectivity*. Geometry information gives the position of its vertices and the connectivity information gives the relationship between its elements. Mesh deformation means modifying the shape of the original object by using control points or external forces. 3D mesh deformation has been a highly active research area in computer graphics. Deformations have widespread usage areas like computer games, computer animations, fluid flow, heat transfer, surgical simulation, cloth simulation, crash test simulations. The major goal in mesh deformations is to establish a good balance between the accuracy of the simulation and the computational cost, which depends on the application.

In order to make deformations realistic and highly accurate, Finite Element Method (FEM) could be used. FEM is a numerical method to find approximate solutions to the problems of engineering and mathematical physics. Typical problems that are solvable by use of the finite element method include structural analysis, heat transfer, fluid flow, mass transport, and electromagnetic potential [**?**].

It is not possible to obtain an analytical solution for problems involving complicated geometries (e.g., 3D organ models), loadings, and material properties.

Analytical solutions generally require the solution of ordinary or partial differential equations. However, they are not generally obtainable because of the problems mentioned above [**?**]. When we incorporate these into the analytical solution, the degree of the partial differential equations becomes so high that the solution is not obtainable. Numerical methods that find approximate solutions are used to overcome this problem. Among these, Rayleigh-Ritz, Galerkin, and Finite Difference methods, are the most common ones. Finite difference method approximates the differential equations with equivalent difference quotients using limits over the domain. In other words, the method approximates the solution of differential equations by using approximations to the derivatives. Rayleigh-Ritz method introduces trial functions like FEM's weight functions. However, it only works for conservative systems and it gets very complicated for complex geometries, such as 3D organ meshes, crash test models. Galerkin method uses weighted residuals to calculate a global stiffness matrix, as FEM does. However, none of these techniques can handle geometrically complex domains. The approximation to the solution becomes very complicated even in simpler domains.

FEM simplifies these calculations by subdividing the given domain into a finite set of subdomains, called *finite elements* [**?**]. The problem becomes easier and solvable over these domains, such as a set of rectangles, triangles, and in our case, tetrahedra. When using FEM for all types of problems; 1D, 2D, 3D, linear or nonlinear, it follows certain steps; finite element discretization, derivation of the element displacement functions, assembly of the elements, imposition of the boundary conditions and solving the system to find an approximate solution of the given domain [**?**].

Surgical simulations require high accuracy, very low error tolerance and real-time interaction that cannot be fully handled with popular deformation techniques, such as regular deformations, Free-form deformation and mass spring system. Numerical solutions that require high accuracy must be used such as finite difference, variational methods and FEM. By far the most popular numerical solution technique is FEM with surgical simulations. Firstly, linear FEM models are used due to faster calculation compared to nonlinear FEM. Cover et al. used surface models to model the system [**?**]. However, surface models are not sufficient

for surgical simulators to perform internal surgical operations. Along with the increase in the computational power of the computers, the work of Bro-nielsen prompted the usage of volumetric models [**?**]. Cavusoglu used nonlinear model's reduction to linear model using linear FEM [**?**]. Most recent surgical simulators use nonlinear FEM [**?**, **?**] because nonlinear FEM is capable of providing realistic predictions of finite deformations of the tissue. Although these recent systems provide real-time simulations, the preprocessing step to calculate the stiffness matrices still takes many hours.

1.1   Contributions

We implemented linear FEM and non-linear FEM by using tetrahedral elements. We used same material properties (constitutive matrices) with linear and nonlinear FEM. In this way, we are able to observe the effect of using the same material with nonlinear geometric properties and compare the results with the results of linear FEM. The contributions can be summarized as follows:

1. We propose a new formulation and finite element solution to the nonlinear 3D elasticity theory.

2. We derived nonlinear stiffness matrices by using the Green-Lagrange strains (large deformation). Green-Lagrange strains are derived directly from the infinitesimal strains (small deformation) by adding the nonlinear terms that are discarded in infinitesimal strain theory.

3. We propose a more comprehensible nonlinear FEM for whom has knowledge about linear FEM since proposed method directly derived from the infinitesimal strains.

4. We use geometric nonlinearity to compare the results of nonlinear FEM with the results of linear FEM.

5. We compare our approach with Pedersen's method to measure the performance and verify the correctness. We achieve 111% speed-up for the

calculation of stiffness matrices and 17% on average for the solution of the whole system, compared to the Pedersen's method.

1.2   Overview of the Thesis

The rest of the thesis is organized as follows. Chapter 2 describes the related work on deformation techniques, Finite Element Method, and the nonlinear analysis. Chapter 3 discusses variational approaches, such as Galerkin, Rayleigh-Ritz and Weighted-Residual methods, and finite difference methods. Chapter 4 explains linear FEM. Chapter 5 describes the nonlinear FEM, including a detailed discussion of the Pedersen's method and the proposed approach. Chapter 6 gives the experimental results obtained using the proposed approach and compares the computational overhead of the proposed approach with that of Pedersen. Chapter 7 gives conclusions and possible future research directions.

Chapter 2

Background and Related Work

2.1 Mesh Deformation Techniques

Two popular deformation techniques are regular deformations [?] and Free-form deformation (FFD) [?]. Regular deformations are nonlinear transformations that twist, taper and bend mesh models. Free-form deformation (FFD) is the first popular deformation technique that is used for deforming solid geometric models in a free-form manner. The FFD approach encloses the object to be deformed in a flexible parallelepiped box that has control points. The bounding box is deformed by moving these control points, and the object inside will be also deformed accordingly. The technique can deform any type of surfaces locally or globally. FFD basically interpolates the mesh's coordinates according to the displacement of the vertices of the bounding box. It can be applied to any 2D or 3D mesh. It is easy to implement and have low computational cost compared to numerical methods. However, FFD is not a physically-based deformation technique; thus, it is not suitable for applications that require physical realism.

Another widely used mesh deformation technique is the mass-spring system. The mass-spring system has widespread usage areas (i.e., cloth, hair and water simulations). It is generally constructed with three types of springs, called structural, shear and bending springs (for 2D deformations); these springs obey the

rule of Hooke's Law [**?**, **?**]. In order to be used in 3D deformations (e.g., surgery simulators), volumetric springs must be added to preserve the volume [**?**]. Mass-spring systems are easy to implement and less costly than numerical methods to simulate dynamic systems in time domain. However, the system reduces the complex stiffness matrix K, which is introduced in Chapter 3, to the mass-spring constant k. Because of this, the potential energy is not preserved and the system cannot handle deformations with high accuracy. They are useful in simulations that require approximate solutions in real time.

2.2 Finite Element Method

Finite Element Method (FEM) is a variational approximation that uses piecewise continuous polynomial basis functions for the numerical solution of boundary value problems and initial boundary value problems governed by partial differential equations or integral equations. Apart from finite difference method, FEM does not use approximated differential equation solutions, which makes FEM more powerful and accurate than the finite difference method. FEM can use all types of variational methods according to requirements of the problem to be solved.

Although the usage of FEM in real world simulations is a relatively new area, the development of FEMs began in the 1940s. Hrennikoff [**?**] and McHenry [**?**] used a lattice of line elements for the solution of the stresses in solids in the field of structural engineering. The energy principles were first introduced to the finite element method by Argyris [**?**] by using structural matrix analysis.

The first solution procedure for 2D FEM was introduced by Turner [**?**]. Turner obtained the solution of 2D triangular and rectangular elements with using stiffness matrices which is the most commonly used technique nowadays for obtaining solutions. Along with the development of computers in 1950s, the work of Turner prompted the usage of equations in matrix form. The term "finite element" was firstly introduced by Clough [**?**]. He showed that the structural analysis

method could be used to solve for the stresses and displacements in continuous structures [?]. 3D FEM was first used by Martin [?], with the development of tetrahedral stiffness matrices. Different types of 3D elements were introduced by Argyris [?].

Up to 1960s, most of the research dealt with linear finite element methods that use infinitesimal strains (small deformation strains). Large deformations and thermal analysis were first considered by Turner [?] and material non-linearities were considered by Gallagher [?].

The variational methods that use FEM were first proposed by Melosh [?]. For the problems that cannot be solved with variational methods, the finite element solution with weighted residual was introduced by Szabo and Lee [?]; it is still a very popular method to achieve the finite element solution.

Finite element models are used frequently to get closer to real world simulations. With the increase in the computational power, finite elements models became popular in computer simulations recently. Due to nonlinear FEM's high computational cost, linear FEMs are introduced to use in deformable models [?]. However, linear models are based on the assumption of small deformation, typically less than 1%, which is not valid for much of the soft tissue deformation. Moreover, linear FEM cannot handle rigid motions either [?]. To address this problem, Cavusoglu [?] proposed a method to determine elasticity parameters of a lumped element (mass-spring) model by approximating the stiffness matrix of the finite element model with the stiffness matrix of the lumped element model. Later, Cavusoglu and Natsupakpong extended the idea of lumped element models from the FEM for triangular, rectangular, and tetrahedral meshes [?]. They extended the classical linear FEM solution with

$$M^e u^e + K^e u^e = 0, \tag{2.1}$$

where K is the stiffness matrix that generalizes the stiffness of Hooke's Law constant k to a matrix and M is the mass matrix to provide damping that comes from lumped element (mass-spring) model.

Nonlinear FEM is a highly-accurate method, which takes into account non-linear constitutive behavior of the materials, as well as large deformation strains. That's why it is very popular for high accuracy computations [**?**]. However, nonlinear models are computationally very intensive and not used for real time simulators. Pedersen used nonlinear large deformation strains for tetrahedral elements [**?**]. However, his methodology to construct stiffness matrices are very complex. This makes already slow nonlinear FEM calculations even slower. We propose a solution that uses Green-Lagrange strains. Our approach is similar to the method of Pedersen; however, the proposed method uses a fast and easy approach to calculate the stiffness matrices.

2.3 General Steps of Finite Element Method

2.3.1 Finite Element Discretization

In the first step, the problem domain is represented by a collection of finite number of subdomains (for 1D set of lines, 2D set of triangles or rectangles), that is called discretization of the domain. Moreover, each subdomain is called an element, and the whole domain is called finite element mesh. Elements are connected to each other with nodes. Subdomain types differ with respect to their solution domain. If it is a 1D problem, string is divided into equal length sub-strings (uniform mesh). If it is a 2D problem, it is triangulated (e.g., using Delaunay triangulation) or divided into small quadrilateral elements. Objects used in simulations, such as car crash tests and surgery simulators, are generally represented by 3D meshes that are divided into tetrahedral or hexahedral elements. The accuracy of the solution can be increased by constructing dense meshes.

2D Delaunay triangulation [**?**] is described as follows. Let V be a set of points in the plane, and T be a triangulation of V. T is a Delaunay triangulation if and only if the circumcircle of any triangle does not contain a point of V in its interior (see Figure 2.1). An arbitrary triangulation can be converted to a Delaunay triangulation using edge flipping operations [**?**].

□

Figure 2.1: The circumscribing circle of any triangle in a Delaunay triangulation contains no other vertices.

A tetrahedralization of a set of vertices V is a set of tetrahedra T, whose interiors do not intersect each other, and whose union is the convex hull of V. Let s be a 3-simplex[1] whose vertices are in V. A sphere S is a circumscribing sphere of s if it passes through all the vertices of s [?]. It can be said that a tetrahedron satisfies the Delaunay property if the circumscribing sphere of the tetrahedron that passes through all of its vertices is empty. Delaunay tetrahedralization is a tetrahedralization where all tetrahedra satisfy this property [?]. Edge flipping can also be applied to an arbitrary tetrahedralization to obtain a Delaunay tetrahedralization.

2.3.2   Element Displacement Functions

After the discretization of the elements, the displacement functions must be defined for finite elements. For each element, the physical process is approximated by using these functions, which relate physical quantities at the nodes [?]. The functions are expressed in terms of the nodal unknowns. These functions can be linear, quadratic or a higher degree polynomial. Quadratic and polynomial equations are time consuming and hard to work with. Linear equations are used frequently because they are easy to work with. The functions are defined within finite element domain and differentiate with respect to element's degree of freedom and strain/displacement relationship.

FEM is derived from the conservation of the potential energy and potential energy is defined by

$$\pi = \mathbf{E}_{strain} + W. \tag{2.2}$$

---

[1]A simplex is the representation of point, line segment, triangle, or tetrahedron with an arbitrary dimension; i.e., 0-simplex is point, 1-simplex is line segment, 2-simplex triangle, and 3-simplex is tetrahedron.

where $\mathbf{E}_{strain}$ is the strain energy of the linear element and W is the work potential. They are given by

$$\mathbf{E}_{strain} = \frac{1}{2} \int_{\Omega^e} \varepsilon^T \sigma dx \text{ and} W = f^e d^T. \tag{2.3}$$

where Ω is the stress, ε is the strain, f is the force vector and u is the displacement for 1D element on x-axis. The elemental stiffness matrix is constructed using the strain energy in Equation 2.3.

2.3.3 Assembly of the Elements

Subdomains are connected to each other with nodes, and the nodal neighbor connections are used to assemble the elements. In this step, boundary conditions are introduced. In numerical simulations, boundary conditions are necessary to make the system solvable. Without limiting or defining the region of the simulation, it is impossible to obtain a solution (the stiffness matrix K will be singular and the inverse of K will not exist). In our case, we use fixed boundary conditions, which ensures that fixed node's positions cannot be changed with the effect of the external forces. After deriving the global stiffness matrix, the unused nodal displacements are cleared from the global stiffness matrix using fixed boundary conditions. At the last step, the system is solved using global force vector (Equation 2.4).

$$\begin{bmatrix} F_1 \\ F_2 \\ \vdots \\ F_n \end{bmatrix} = \begin{bmatrix} K_{1,1} & K_{1,2} & \cdots & K_{1,n} \\ K_{2,1} & K_{2,2} & \cdots & K_{2,n} \\ \vdots & \vdots & \ddots & \vdots \\ K_{m,1} & K_{m,2} & \cdots & K_{m,n} \end{bmatrix} \begin{bmatrix} d_1 \\ d_2 \\ \vdots \\ d_n \end{bmatrix}. \tag{2.4}$$

f is the force vector and d is the unknown displacements.

2.3.4 Convergence of the Solution and the Error Estimation

This part differentiates with respect to the FEM methodology used. If linear FEM is used, the solution may be compared with an analytical solution (if an analytical solution is obtainable). If nonlinear FEM is used, the solution procedure continues until the desired accuracy is reached. In nonlinear FEM, the solution involves Newton-Raphson method that reduces the error at each iteration. If an analytical solution exists, the error analysis can be done by comparing the approximate solution with the analytical solution. When the exact solution is not known, a conditional linear FEM error estimation can be done by taking the non-linear solution as the basis, and comparing the linear solution with it. Moreover, an independent error analysis can be done by using the approximate results and comparing the displacements of the element for two meshes with mesh densities d and $\frac{d}{2}$. We have

$$\| u^d - u^{\frac{d}{2}} \| = \| (u - u^{\frac{d}{2}}) + (u^d - u) \| . \tag{2.5}$$

By triangular inequality for the energy norm [?]

$$\| u^d - u^{\frac{d}{2}} \| \leq \| (u - u^{\frac{d}{2}}) \| + \| (u^d - u) \|. \tag{2.6}$$

Assuming both finite element solutions are convergent, we can express the errors as

$$\begin{aligned} \| u^d - u \| &= O(h^m) \text{ and} \\ \| u - u^{\frac{d}{2}} \| &= O(h^p). \end{aligned} \tag{2.7}$$

The rate of convergence for Equation 2.7 becomes $m > p$. As the mesh becomes denser, p becomes very small as compared to m. Thus, we obtain

$$\| u^d - u^{\frac{d}{2}} \| = C \| (u - u^{\frac{d}{2}}) \| . \tag{2.8}$$

Using Equation 2.8, we can assume that our solution u is valid and converges to the exact solution. In this case, the difference of $u^d - u^{\frac{d}{2}}$, decreases with the mesh refinement.

The final goal is to interpret and analyze the results for use in the design-analysis process. The mesh model can be visualized using tools such as Autodesk's Mechanical Simulation Sofware [?]. We used our own visualization program that is based on OpenGL to display the mesh model.

2.4   Advantages of Finite Element Methods

As explained before, FEM has advantages over the analytical solutions and other approximate solutions. Most important advantages of FEM are [?]:

1. FEM can handle very complex geometries;

2. FEM can be used for different kinds of problem domains (mechanic, fluid, heat, magnetic, etc.);

3. FEM can handle different kind of materials easily therefore material properties are easily added to the element equations;

4. FEM can handle a variety of boundary conditions (fixed, linear, time varying boundary conditions);

5. Nonlinearities are handled better;

6. FEM can easily increase the accuracy by changing the density of the model.

2.5   Nonlinear Analysis

The FEM technique used differs according to the requirements of the application (e.g., small or large deformations). Linear FEM is used for small deformations. The linear strain is easy to calculate and does not involve the solution of the nonlinear equations. Hence, it does not involve numerical methods, like Newton-Raphson, that is generally used for approximate solutions to the nonlinear systems of equations. However, they lack realism and accuracy required in applications, such as soft tissue deformations in surgical simulations [**?**, **?**]. With the introduction of non-linear strains, large deformations are handled better; e.g. the high amplitude bending and twisting behavior.

Linear solutions are generally approximations to the nonlinear solutions to simplify the solution process and make computation less costly. In most of the applications, the linear solution may provide acceptable results [**?**]. However, the applications that require high accuracy and very low error tolerance cannot be handled with the linear solution (e.g., surgical simulators, aeronautics applications, crash test applications). Nonlinear analysis is used commonly in the following areas [**?**]:

1. Simulation of the physical phenomena (fluid, heat, magnetic field analysis);

2. Simulation of the true material behavior (material nonlinearities, plastic deformation);

3. Applications of aeronautics, defense industry and nuclear systems that require very high accuracy and low error tolerance;

4. Applications of civil engineering to describe the large displacements (steel, concrete and cable constructions);

5. Concrete constructions or soil mechanics;

6. Manufacturing of concrete (heat analysis because of chemical reactions);

7. Automobile industry simulations (crash tests and simulations);

8. Medical simulations (i.e., medical visualization, analysis and surgical simulators).

There are different types of nonlinearities that change the solution process. The solution methods have to be adjusted with respect to the type of inherent nonlinearity. Nonlinearities arise from two main sources; *material* and *geometric* nonlinearities [**?**]. Material nonlinearities are caused by constitutive behavior of the material itself, such as plastic materials. Geometric nonlinearities are caused by geometric displacement of the material, such as strain-displacement relations.

Chapter 3

Numerical Techniques

This chapter first introduces the preliminaries for variational methods and finite element method. Then it explains the variational approaches, such as Galerkin, Rayleigh-Ritz and Weighted-Residual methods, and finite difference methods.

3.1   Preliminaries

3.1.1   Boundary Conditions

Boundary conditions are the additional constraints in order to solve a differential equation. For example, for the differential equation

$$-u'' - 2xu' + 2u = f(x), \tag{3.1}$$

the boundary conditions can be defined as

$$u(0) = 0, u(1) = ln(0.5). \tag{3.2}$$

When solving the problems with FEM over the domain boundary conditions

must be satisfied. Otherwise stiffness matrix K will be singular and solution of the system does not exist. This means the system is unstable. Two types of boundary conditions are used in FEM. Mostly homogeneous boundary conditions (fixed boundary conditions) are used. They ensures that the nodes are fixed and does not move with the effect of the external forces. We also use fixed boundary conditions in our proposed solution. Nonhomogeneous boundary conditions occur where finite nonzero values of displacement are specified, such as the settlement of the support points [?].

3.1.2 Boundary Value Problem

Boundary value problem (BVP) is a type of partial differential problem that uses boundary conditions. In this type of problems its derivatives $u'(0) = 1$ and dependent variables $u(0) = c$ can take special values on the boundary. Hence, solution to the problem must satisfy boundary conditions [?]. An example BVP is given by

$$-u'' = x, 0 < x < 1, u(0) = 0, u'(0) = 1. \tag{3.3}$$

3.1.3 Variational Operator

$$f(x) = -(ku)' + bu' + cu. \tag{3.4}$$

The function $f(x)$ in Equation 3.4 is dependent on u and u' for a fixed value of the independent variable x. The change αv in u is called the variation of u, where v is a function and α is constant [?]. Moreover, this variation operation is represented by $\delta u = v$, and δ is called the variational operator. Mostly, variation is used to achieve weak formulations as described as follows.

3.1.4 Weak Formulations

The weak form of a differential equation is the weighted integral statement of the differential equation that is used in variational methods, distributed among the dependent variable and the weight or trial functions [?]. The construction of the weak formulation is achieved in three steps.

Consider a BVP by

$$-(ku')' + bu' + cu = f(x), 0 < x < L, u(0) = u(L) = 0. \tag{3.5}$$

The residual is defined by

$$r(\hat{u}) = -(ku')' + bu' + cu - f(x). \tag{3.6}$$

In the first step, weight functions ψ are selected to satisfy the following boundary conditions

$$\psi(0) = \psi(L) = 0. \tag{3.7}$$

In the second step, the residual is multiplied with the weight function ψ and integrated over the domain.

$$u = \int_0^L \psi r(\hat{u}) dx = 0. \tag{3.8}$$

If $\hat{u}$ is the solution of the problem, $r(\hat{u}) = 0 \Rightarrow \hat{u} = u$. Equation 3.8 is extended by

$$u = \int_0^L \psi(-(ku')' + bu' + cu - f(x)) dx = 0. \tag{3.9}$$

The term ψ in Equation 3.9 is called the weight function or weighted-residuals [?]. In the last step, the weight function is extended by integration by parts:

$$\int_0^L -\psi(x)(k(\hat{u}'))'dx = -ku\psi|_0^L + \int_0^L k\hat{u}'v'dx = \int_0^L k\hat{u}'\psi' \text{ and} \qquad (3.10)$$

$$-ku\psi|_0^L = 0, \qquad (3.11)$$

since $\psi(0) = \psi(L) = 0$. Finally, the weak form or variational form of Equation 3.5 becomes

$$\int_0^L (k\hat{u}'\psi' + b\hat{u}'\psi + c\hat{u}\psi - f\psi)dx = 0. \qquad (3.12)$$

3.1.5   Weighted Integral Forms and Residuals

In FEM and variational methods, the solution is represented by

$$u = \sum_{k=1}^N u_k\psi_k. \qquad (3.13)$$

When we substitute Equation 3.13 into differential equations, it does not always result in giving the linearly dependent coefficient of u_k. In that case there is not any actual solution to N number of equations. Instead of actual solution, approximate solution to u is found by using weighted integrals and residuals in order to find the unknown coefficients [?].

$$u = \int_0^L \psi r dx = 0, \qquad (3.14)$$

where ψ is the weight function and r is the residual. This weight function differs by what kind of variational method is used to solve the problem.

3.2   Variational Methods

Variational method is a general method that can be used to achieve an approximate solution for both structural and nonstructural problems by using weighted integral statements or trial functions [?].

3.2.1   Weighted-Residual Methods

Weighted-residual method seeks the approximate solution to the system by using weighted integral statements [?]. Weighted-residual method is the generalization of Rayleigh-Ritz Method. It does not operate in weak form, since weak form does not always exist. Moreover, test functions that form weighted integral statements must satisfy boundary conditions and must be linearly independent. For example, for the problem

$$-(ku')' + bu' + cu = f, u(0) = u(L), \tag{3.15}$$

the residual is defined as

$$r(u) = -(ku')' + bu' + cu - f. \tag{3.16}$$

When we multiply the residual with the test functions, we obtain

$$\int_0^L vr(u)dx = 0, \tag{3.17}$$

where $0 < x < L$ and the weight functions are defined as

$$v_N(x) = \sum_{i=1}^N \beta_i \psi_i(x) \text{ and}$$
$$u_N(x) = \sum_{j=1}^N \alpha_i \phi_j(x). \tag{3.18}$$

The choice of the weight functions and the approximation functions determine
the type of the variational method. The trial functions ($\phi_i(x)$ and $\psi_i(x)$) must
be linearly independent. If Equation 3.18 is substituted into Equation 3.16, we
get

$$\sum_{i=1}^{N} \psi_i \left(\sum_{j=1}^{N} (K_{ij} + B_{ij} + C_{ij})\phi_j - f_i \right) = 0 \quad \text{and} \tag{3.19}$$

$$\sum_{j=1}^{N} K_{ij}\alpha_j = f_i, \quad \text{where } i = 1, 2, \dots, N. \tag{3.20}$$

If the weight functions (ψ_i) and test functions (ϕ_i) are the same, Equation 3.19
leads to Galerkin's Method (Equation 3.20), which is generally used to construct
FEM's test functions.

3.2.2 Rayleigh-Ritz Method

The Rayleigh-Ritz method uses trial or weight functions to find an approximate
solution to the system. These trial functions are linearly independent set of finite
series [?].

$$u_N(x) = \sum_{k=1}^{N} \alpha_k \phi_k(x), \tag{3.21}$$

where α_k constants are called Ritz coefficients. The trial functions must satisfy
the condition $\sum_{k=1}^{N} \alpha_k \phi_k(x) = u_0$ so that N linearly independent equations are ob-
tained. The prescribed functions ($\phi_k(x)$) are given to satisfy the given boundary
conditions, and they may grow exponentially in the equation according to the
test function's choice,

$$\{u\} = \begin{Bmatrix} \alpha_1 x \\ \alpha_2 x^2 \\ \alpha_3 x^3 \\ \vdots \\ \alpha_n x^n \end{Bmatrix}. \tag{3.22}$$

From the given trial functions, the stiffness matrix is computed and the system of linear equations is solved. However, guessing trial functions in a way that satisfy the boundary conditions for complex objects, such as human organ models, is almost impossible. Even if these conditions are satisfied, solving the system of equations is very difficult because of the high degree of freedom. For example, for a thousand-node mesh, the polynomial for the trial function may become $\alpha_n x^{1000}$.

For problem $-(ku')' + bu' + cu = f$, the first residual is defined as

$$r(u) = -(ku')' + bu' + cu - f. \tag{3.23}$$

When we multiply the residual with test functions, we obtain

$$\int_0^L \psi r(u) dx = 0. \tag{3.24}$$

Combining Equations 3.23 and 3.24, we obtain the solution to the problem:

$$\int_0^L (ku'v' + buv' + cuv - fv) dx = 0. \tag{3.25}$$

Equation 3.25 is obtained by weakening Equation 3.23.

We cannot use Galerkin's method or Rayleigh-Ritz method directly to solve complex systems. The problem domain must be divided into subdomains (discretization) and an appropriate variational method must be used in order to solve complex problems. Another variational technique, Petrov-Galerkin method, uses

$\psi_i \neq \phi_i$, and least-squares method uses $\psi_i = A(\phi_i)$ as a weight function. Zhu and Gortler use least squares method to deform 3D models [**?**].

3.3 Finite Difference Method

Finite difference method uses finite difference equations instead of partial differential equations (PDEs) like FEM uses. It approximates the PDEs with finite difference equations [**?**]. It is based on simplifications of elasticity theory [**?**]. It follows similar steps with FEM:

1. Discretization,

2. Approximating the differential equations with difference equations, and

3. Solving the system in domain.

The differential equations can be approximated as in the following difference equations:

$$u_i' \cong \frac{u_{i+1} - u_i}{h}, \tag{3.26}$$

$$u_i' \cong \frac{u_i - u_{i-1}}{h}, \tag{3.27}$$

$$u_i' \cong \frac{u_{i+1} - u_{i-1}}{2h}, \tag{3.28}$$

where h is the element distance in 1D. Equation 3.26 is forward-difference formula, Equation 3.27 is backward-difference formula and Equation 3.28 is central-difference formula. These equations are found by using Taylor's series expansion

$$u_{i+1} = u_i + h u_i' + \frac{h^2}{2!} u_i'' + \frac{h^3}{3!} u_i''' + O(h^4). \tag{3.29}$$

In this case, $O(h^4)$ is the error if we do not want to expand the series more. Generally, the expansion is left at $\frac{h^2}{2!}u_i''$ to keep the difference operation simple and less costly.

In the finite element method, we relate stresses, forces or strains that are in the system by using partial differential equations. On the other hand, in the finite-difference method, we replace these PDEs with simple difference operators. It can be said that FEM is superior to the finite difference method in terms of accuracy and complexity.

Chapter 4

Linear Finite Element Method

This chapter describes in detail the linear FEM method, development of small deformation strains that lead to linear FEM, the stiffness matrix, and the solution of the linear FEM.

4.1 Linear FEM Using Tetrahedral Elements

Most of the linear FEM methods for 3D tetrahedral elements consist of five stages:

1. Tetrahedralization;

2. Construction of elemental stiffness matrices;

3. Assembly of elemental stiffness matrices and force vectors;

4. Applying boundary conditions;

5. Solving the linear system that gives unknown nodal displacements.

4.1.1   Tetrahedralization

We use same tetrahedralized meshes for both linear and non-linear solutions to provide integrity and make a better analysis for our experiments. We use the Application Programming Interface of TetGen [**?**] as a tetrahedral mesh generator and integrated it into our implementation. The tetrahedralization process produces the nodal positions and the elements for each node. We use nodal positions to construct elemental stiffness matrices, and element's nodal information to assemble the elemental stiffness matrices to form the global stiffness matrix.

4.1.2   Construction of Elemental Stiffness Matrices

□

Figure 4.1: Tetrahedral element

We use tetrahedral elements for modeling meshes in the experiments (Figure 4.1). Overall, there are 12 unknown nodal displacements in a tetrahedral element. They are given by [**?**]

$$\left\{d\right\} = \left\{u(x, y, z)\right\} = \begin{Bmatrix} u_1 \\ v_1 \\ w_1 \\ \vdots \\ u_4 \\ v_4 \\ w_4 \end{Bmatrix}. \tag{4.1}$$

In global coordinates, we represent displacements by linear function by

$$u^e(x, y, z) = c_1 + c_2 x + c_3 y + c_4 z. \tag{4.2}$$

For all 4 vertices, Equation 4.2 is extended as

$$
\begin{bmatrix} 1 & x_1 & y_1 & z_1 \\ 1 & x_2 & y_2 & z_2 \\ 1 & x_3 & y_3 & z_3 \\ 1 & x_4 & y_4 & z_4 \end{bmatrix} \begin{Bmatrix} c_1 \\ c_2 \\ c_3 \\ c_4 \end{Bmatrix} = \begin{Bmatrix} u_1 \\ u_2 \\ u_3 \\ u_4 \end{Bmatrix}. \tag{4.3}
$$

Constants c_n can be found as

$$
c_n = v^{-1} u_n, \tag{4.4}
$$

where v^{-1} is given by

$$
v^{-1} = \frac{1}{det(v)} \begin{bmatrix} \alpha_1 & \alpha_2 & \alpha_3 & \alpha_4 \\ \beta_1 & \beta_2 & \beta_3 & \beta_4 \\ \gamma_1 & \gamma_2 & \gamma_3 & \gamma_4 \\ \delta_1 & \delta_2 & \delta_3 & \delta_4 \end{bmatrix}. \tag{4.5}
$$

$det(v)$ is $6V$, where V is the volume of the tetrahedron. If we substitute Equation 4.4 into Equation 4.2, we obtain

$$
u^e(x, y, z) = \frac{1}{6V^e} \begin{bmatrix} 1 & x & y & z \end{bmatrix} \begin{bmatrix} \alpha_1 & \alpha_2 & \alpha_3 & \alpha_4 \\ \beta_1 & \beta_2 & \beta_3 & \beta_4 \\ \gamma_1 & \gamma_2 & \gamma_3 & \gamma_4 \\ \delta_1 & \delta_2 & \delta_3 & \delta_4 \end{bmatrix} \begin{Bmatrix} u_1 \\ u_2 \\ u_3 \\ u_4 \end{Bmatrix}. \tag{4.6}
$$

α, β, γ, δ and the volume V are calculated by

$$
\alpha_1 = \begin{vmatrix} x_2 & y_2 & z_2 \\ x_3 & y_3 & z_3 \\ x_4 & y_4 & z_4 \end{vmatrix}, \quad \alpha_2 = - \begin{vmatrix} x_1 & y_1 & z_1 \\ x_3 & y_3 & z_3 \\ x_4 & y_4 & z_4 \end{vmatrix}, \quad \alpha_3 = \begin{vmatrix} x_1 & y_1 & z_1 \\ x_2 & y_2 & z_2 \\ x_4 & y_4 & z_4 \end{vmatrix}, \quad \alpha_4 = - \begin{vmatrix} x_1 & y_1 & z_1 \\ x_2 & y_2 & z_2 \\ x_3 & y_3 & z_3 \end{vmatrix}
$$
$$
\tag{4.7}
$$

$$\beta_1 = - \begin{vmatrix} 1 & y_2 & z_2 \\ 1 & y_3 & z_3 \\ 1 & y_4 & z_4 \end{vmatrix}, \quad \beta_2 = \begin{vmatrix} 1 & y_1 & z_1 \\ 1 & y_3 & z_3 \\ 1 & y_4 & z_4 \end{vmatrix}, \quad \beta_3 = - \begin{vmatrix} 1 & y_1 & z_1 \\ 1 & y_2 & z_2 \\ 1 & y_4 & z_4 \end{vmatrix}, \quad \beta_4 = \begin{vmatrix} 1 & y_1 & z_1 \\ 1 & y_2 & z_2 \\ 1 & y_3 & z_3 \end{vmatrix}$$

$$(4.8)$$

$$\gamma_1 = \begin{vmatrix} 1 & x_2 & z_2 \\ 1 & x_3 & z_3 \\ 1 & x_4 & z_4 \end{vmatrix}, \quad \gamma_2 = - \begin{vmatrix} 1 & x_1 & z_1 \\ 1 & x_3 & z_3 \\ 1 & x_4 & z_4 \end{vmatrix}, \quad \gamma_3 = \begin{vmatrix} 1 & x_1 & z_1 \\ 1 & x_2 & z_2 \\ 1 & x_4 & z_4 \end{vmatrix}, \quad \gamma_4 = - \begin{vmatrix} 1 & x_1 & z_1 \\ 1 & x_2 & z_2 \\ 1 & x_3 & z_3 \end{vmatrix}$$

$$(4.9)$$

$$\delta_1 = - \begin{vmatrix} 1 & x_2 & y_2 \\ 1 & x_3 & y_3 \\ 1 & x_4 & y_4 \end{vmatrix}, \quad \delta_2 = \begin{vmatrix} 1 & x_1 & y_1 \\ 1 & x_3 & y_3 \\ 1 & x_4 & y_4 \end{vmatrix}, \quad \delta_3 = - \begin{vmatrix} 1 & x_1 & y_1 \\ 1 & x_2 & y_2 \\ 1 & x_4 & y_4 \end{vmatrix}, \quad \delta_4 = \begin{vmatrix} 1 & x_1 & y_1 \\ 1 & x_2 & y_2 \\ 1 & x_3 & y_3 \end{vmatrix}$$

$$(4.10)$$

$$6V = \begin{vmatrix} 1 & x_i & y_i & z_i \\ 1 & x_j & y_j & z_j \\ 1 & x_k & y_k & z_k \\ 1 & x_l & y_l & z_l \end{vmatrix}$$

$$(4.11)$$

Because of the differentials in strain calculation, α is not used in the following stages. If we expand Equation 4.6, we obtain

$$u^e(x, y, z) =$$
$$\frac{1}{6V^e} \begin{bmatrix} \alpha_1 + \beta_1 x + \gamma_1 y + \delta_1 z \\ \alpha_2 + \beta_2 x + \gamma_2 y + \delta_2 z \\ \alpha_3 + \beta_3 x + \gamma_3 y + \delta_3 z \\ \alpha_4 + \beta_4 x + \gamma_4 y + \delta_4 z \end{bmatrix} \begin{bmatrix} u(x,y,z)_1 & u(x,y,z)_2 & u(x,y,z)_3 & u(x,y,z)_4 \end{bmatrix}$$

$$(4.12)$$

For tetrahedral elements, to express displacements in simpler form, shape functions are introduced $(\psi_1, \psi_2, \psi_3, \psi_4)$. They are given by

$$
\begin{aligned}
\psi_1 &= \tfrac{1}{6V} \left(\alpha_1 + \beta_1 x + \gamma_1 y + \delta_1 z\right) u(x, y, z)_1 \\
\psi_2 &= \tfrac{1}{6V} \left(\alpha_2 + \beta_2 x + \gamma_2 y + \delta_2 z\right) u(x, y, z)_2 \\
\psi_3 &= \tfrac{1}{6V} \left(\alpha_3 + \beta_3 x + \gamma_3 y + \delta_3 z\right) u(x, y, z)_3 \\
\psi_4 &= \tfrac{1}{6V} \left(\alpha_4 + \beta_4 x + \gamma_4 y + \delta_4 z\right) u(x, y, z)_4
\end{aligned}
\tag{4.13}
$$

The next step is to find the infinitesimal strains that are used to calculate the global stiffness matrix. Figure 4.2 shows that the element edge that lies on x-axis AB becomes $A'B'$. The engineering normal strain is calculated as the change in the length of the line [?]:

□

Figure 4.2: 2D element before and after deformation [?].

$$
\varepsilon_x = \frac{A'B' - AB}{AB}
\tag{4.14}
$$

and

$$
AB = dx.
\tag{4.15}
$$

The elemental edge dx that is initially parallel to the x-axis is deformed as $(A'B')^2$ (cf. Equation 4.16). The final length can be evaluated by

$$
\begin{aligned}
(A'B')^2 &= \left(dx + \tfrac{\partial u_x}{\partial x} dx\right)^2 + \left(\tfrac{\partial u_y}{\partial x} dx\right)^2, \\
(A'B')^2 &= dx \left[1 + 2\left(\tfrac{\partial u_x}{\partial x}\right) + \left(\tfrac{\partial u_x}{\partial x}\right)^2 + \left(\tfrac{\partial u_y}{\partial x}\right)^2\right].
\end{aligned}
\tag{4.16}
$$

By neglecting the higher order terms in Equation 4.16, the 2D strains are defined by

$$\begin{aligned}
\varepsilon_{xx} &= \frac{\partial u_x}{\partial x} \\
\varepsilon_{yy} &= \frac{\partial u_y}{\partial y} \\
\gamma_{xy} &= \frac{1}{2}\left(\frac{\partial u_x}{\partial y} + \frac{\partial u_y}{\partial x}\right)
\end{aligned} \tag{4.17}$$

After finding the 2D strains, it is straightforward to expand it to the 3D case by

$$\begin{aligned}
\varepsilon_{zz} &= \frac{\partial u_z}{\partial z} \\
\gamma_{zx} &= \frac{1}{2}\left(\frac{\partial u_z}{\partial x} + \frac{\partial u_x}{\partial z}\right) \\
\gamma_{yz} &= \frac{1}{2}\left(\frac{\partial u_y}{\partial z} + \frac{\partial u_z}{\partial y}\right)
\end{aligned} \tag{4.18}$$

Infinitesimal strains with 3D element are given by

$$\{\varepsilon\} = \begin{Bmatrix} \varepsilon_{xx} \\ \varepsilon_{yy} \\ \varepsilon_{zz} \\ 2\gamma_{xy} \\ 2\gamma_{zx} \\ 2\gamma_{yz} \end{Bmatrix} = \begin{Bmatrix} \frac{\partial u_x}{\partial x} \\ \frac{\partial u_y}{\partial y} \\ \frac{\partial u_z}{\partial z} \\ \frac{\partial u_x}{\partial y} + \frac{\partial u_y}{\partial x} \\ \frac{\partial u_z}{\partial x} + \frac{\partial u_x}{\partial z} \\ \frac{\partial u_y}{\partial z} + \frac{\partial u_z}{\partial y} \end{Bmatrix}. \tag{4.19}$$

After finding strains, these equations are combined with shape functions to find matrix $[B]$:

$$\{\varepsilon\} = [B]\{d\}. \tag{4.20}$$

Using Equations 4.13 for displacements, we can evaluate the partial derivatives of the shape functions as follows:

$$\frac{\partial u_x}{\partial x} = \frac{\partial}{\partial x}(\psi_1 + \psi_2 + \psi_3 + \psi_4) = \frac{1}{6V}(\beta_1 u_1 + \beta_2 u_2 + \beta_3 u_3 + \beta_4 u_4)$$

$$\frac{\partial u_y}{\partial y} = \frac{1}{6V}(\gamma_1 v_1 + \gamma_2 v_2 + \gamma_3 v_3 + \gamma_4 v_4)$$

$$\frac{\partial u_z}{\partial z} = \frac{1}{6V}(\delta_1 w_1 + \delta_2 w_2 + \delta_3 w_3 + \delta_4 w_4)$$

$$\frac{\partial u_x}{\partial y} + \frac{\partial u_y}{\partial x} = \frac{1}{6V}(\gamma_1 u_1 + \gamma_2 u_2 + \gamma_3 u_3 + \gamma_4 u_4 + \beta_1 v_1 + \beta_2 v_2 + \beta_3 v_3 + \beta_4 v_4)$$

$$\frac{\partial u_z}{\partial x} + \frac{\partial u_x}{\partial z} = \frac{1}{6V}(\beta_1 w_1 + \beta_2 w_2 + \beta_3 w_3 + \beta_4 w_4 + \delta_1 u_1 + \delta_2 u_2 + \delta_3 u_3 + \delta_4 u_4)$$

$$\frac{\partial u_y}{\partial z} + \frac{\partial u_z}{\partial y} = \frac{1}{6V}(\delta_1 v_1 + \delta_2 v_2 + \delta_3 v_3 + \delta_4 v_4 + \gamma_1 w_1 + \gamma_2 w_2 + \gamma_3 w_3 + \gamma_4 w_4)$$

$$(4.21)$$

Using Equations 4.21 for the 1st node, we obtain the submatrix $[B_1]$ of $[B]$ as

$$[B_1] = \begin{bmatrix} \frac{\partial u_x}{\partial x} & 0 & 0 \\ 0 & \frac{\partial u_y}{\partial y} & 0 \\ 0 & 0 & \frac{\partial u_z}{\partial z} \\ \frac{\partial u_x}{\partial y} & \frac{\partial u_y}{\partial x} & 0 \\ \frac{\partial u_z}{\partial x} & 0 & \frac{\partial u_x}{\partial z} \\ 0 & \frac{\partial u_y}{\partial z} & \frac{\partial u_z}{\partial y} \end{bmatrix} \begin{Bmatrix} u_1 \\ v_1 \\ w_1 \end{Bmatrix}. \qquad (4.22)$$

Using Equations 4.21 and 4.22, $\{\varepsilon\}$ can be written as

$$\{\varepsilon\} = [B]\{d\} = \begin{bmatrix} \beta_1 & 0 & 0 & \beta_2 & 0 & 0 & \beta_3 & 0 & 0 & \beta_4 & 0 & 0 \\ 0 & \gamma_1 & 0 & 0 & \gamma_2 & 0 & 0 & \gamma_3 & 0 & 0 & \gamma_4 & 0 \\ 0 & 0 & \delta_1 & 0 & 0 & \delta_2 & 0 & 0 & \delta_3 & 0 & 0 & \delta_4 \\ \gamma_1 & \beta_1 & 0 & \gamma_2 & \beta_2 & 0 & \gamma_3 & \beta_3 & 0 & \gamma_4 & \beta_4 & 0 \\ \delta_1 & 0 & \beta_1 & \delta_2 & 0 & \beta_2 & \delta_3 & 0 & \beta_3 & \delta_4 & 0 & \beta_4 \\ 0 & \delta_1 & \gamma_1 & 0 & \delta_2 & \gamma_2 & 0 & \delta_3 & \gamma_3 & 0 & \delta_5 & \gamma_5 \end{bmatrix} \begin{Bmatrix} u_1 \\ v_1 \\ w_1 \\ u_2 \\ v_2 \\ w_2 \\ u_3 \\ v_3 \\ w_3 \\ u_4 \\ v_4 \\ w_4 \end{Bmatrix}.$$

$$(4.23)$$

In Equation 2.3, the engineering stress vector $\{\sigma\}$ is related to the strain vector $\{\varepsilon\}$ by

$$\begin{aligned}
\{\sigma\} &= [E]\{\varepsilon\}, \\
\{\sigma\} &= [E][B]\{d\},
\end{aligned} \tag{4.24}$$

where $[E]$ is the material property matrix (constitutive matrix) defined by

$$[E] = \frac{\epsilon}{(1+\nu)(1-2\nu)}
\begin{bmatrix}
(1-\nu) & \nu & \nu & 0 & 0 & 0 \\
\nu & (1-\nu) & \nu & 0 & 0 & 0 \\
\nu & \nu & (1-\nu) & 0 & 0 & 0 \\
0 & 0 & 0 & \frac{(1-2\nu)}{2} & 0 & 0 \\
0 & 0 & 0 & 0 & \frac{(1-2\nu)}{2} & 0 \\
0 & 0 & 0 & 0 & 0 & \frac{(1-2\nu)}{2}
\end{bmatrix}, \tag{4.25}$$

where ϵ is the Young's modulus and ν is the Poisson's ratio. Young's modulus describes the elastic properties of a solid undergoing tension or compression. Poisson's ratio is the ratio of transverse strain (perpendicular to the applied load), to the longitudinal strain (in the direction of the applied load) [?]. From the conservation of the potential energy, substituting Equations 4.20 and 4.24 into Equation 2.3, we obtain the element stiffness matrix

$$[k] = \int \int \int \{d\}^T [B]^T [E][B]\{d\} dx \ dy \ dz. \tag{4.26}$$

As seen from Equations 4.22 and 4.25, the matrices $[B]$ and $[E]$ are constant for a tetrahedral element, so that Equation 4.26 is rewritten as

$$[k] = \{d\}^T [B]^T [E][B]\{d\} V. \tag{4.27}$$

With the introduction of the nodal forces per element,

$$\{f\} = \begin{Bmatrix} f_{1x} \\ f_{1y} \\ f_{1z} \\ \vdots \\ f_{4x} \\ f_{4y} \\ f_{4z} \end{Bmatrix} \{d\}^T. \tag{4.28}$$

With the equilibrium equation and the cancellation of the $\{d\}^T$, the whole system for one element reduces to

$$K^e \{d\}^e = \{f\}^e. \tag{4.29}$$

By substituting $\{d\}$ with u, we obtain [**?**]:

$$K^e u^e = f^e. \tag{4.30}$$

4.1.3   Assembly of Elemental Stiffness Matrices

□

Figure 4.3: A tetrahedral mesh with two elements

We apply assembly process using the element's nodal information (which nodes belong to which elements). The size of elemental stiffness matrix is 12×12 (the tetrahedron has four nodes and it is three-dimensional). The size of global stiffness matrix is $3N \times 3N$, where N is the total number of nodes of the whole system. In order to complete the assembly process, all elemental stiffness matrices must be copied to the correct index of the global stiffness matrix. The assembly operation is described by using two elements (Figure 4.3) as an example. The stiffness matrices of the first and second elements are given as

$$K_1 = \begin{bmatrix} k_{1,1}^1 & k_{1,2}^1 & k_{1,3}^1 & \cdots & k_{1,12}^1 \\ k_{2,1}^1 & k_{2,2}^1 & k_{2,3}^1 & \cdots & k_{2,12}^1 \\ k_{3,1}^1 & k_{3,2}^1 & k_{3,3}^1 & \cdots & k_{3,12}^1 \\ \vdots & \vdots & \vdots & \vdots & \vdots \\ k_{12,1}^1 & k_{12,2}^1 & k_{12,3}^1 & \cdots & k_{12,12}^1 \end{bmatrix} \text{ and } K_2 = \begin{bmatrix} k_{1,1}^2 & k_{1,2}^2 & k_{1,3}^2 & \cdots & k_{1,12}^2 \\ k_{2,1}^2 & k_{2,2}^2 & k_{2,3}^2 & \cdots & k_{2,12}^2 \\ k_{3,1}^2 & k_{3,2}^2 & k_{3,3}^2 & \cdots & k_{3,12}^2 \\ \vdots & \vdots & \vdots & \vdots & \vdots \\ k_{12,1}^2 & k_{12,2}^2 & k_{12,3}^2 & \cdots & k_{12,12}^2 \end{bmatrix}.$$

$$(4.31)$$

It can be seen from Figure 4.3 that Nodes 2, 3 and 4 belong to both Element 1 and Element 2. When we assemble the elements, these shared values in the global stiffness matrix (5 nodes, 15×15 matrix) come from both Element 1 and Element 2. The elements are assembled using Algorithm 1, which constructs the global stiffness matrix K (see Equation 4.32).

Algorithm 1 Assembly of the Elements

---
    for i = 1 to N **do**

        $f_{BI} = ((1^{st} \text{ node of } i^{th} \text{ element - 1}) \times 3) + 1$

        $s_{BI} = ((2^{nd} \text{ node of } i^{th} \text{ element - 1}) \times 3) + 1$

        $t_{BI} = ((3^{rd} \text{ node of } i^{th} \text{ element - 1}) \times 3) + 1$

        $r_{BI} = ((4^{th} \text{ node of } i^{th} \text{ element - 1}) \times 3) + 1$

        $K[f_{BI}{:}f_{BI}+2, f_{BI}{:} f_{BI}+2] \mathrel{+}= K_i[1{:}3,1{:}3]$

        $K[f_{BI}{:}f_{BI}+2, s_{BI}{:} s_{BI}+2] \mathrel{+}= K_i[1{:}3,4{:}6]$

        $K[f_{BI}{:}f_{BI}+2, t_{BI}{:} t_{BI}+2] \mathrel{+}= K_i[1{:}3,7{:}9]$

        $K[f_{BI}{:}f_{BI}+2, r_{BI}{:} r_{BI}+2] = K_i[1{:}3,10{:}12]$

        $K[s_{BI}{:}s_{BI}+2, f_{BI}{:} f_{BI}+2] \mathrel{+}= K_i[4{:}6,1{:}3]$

        $K[s_{BI}{:}s_{BI}+2, s_{BI}{:} s_{BI}+2] \mathrel{+}= K_i[4{:}6,4{:}6]$

        $K[s_{BI}{:}s_{BI}+2, t_{BI}{:} t_{BI}+2] \mathrel{+}= K_i[4{:}6,7{:}9]$

        $K[s_{BI}{:}s_{BI}+2, r_{BI}{:} r_{BI}+2] \mathrel{+}= K_i[4{:}6,10{:}12]$

        $K[t_{BI}{:}t_{BI}+2, f_{BI}{:} f_{BI}+2] \mathrel{+}= K_i[7{:}9,1{:}3]$

        $K[t_{BI}{:}t_{BI}+2, s_{BI}{:} s_{BI}+2] \mathrel{+}= K_i[7{:}9,4{:}6]$

        $K[t_{BI}{:}t_{BI}+2, t_{BI}{:} t_{BI}+2] \mathrel{+}= K_i[7{:}9,7{:}9]$

        $K[t_{BI}{:}t_{BI}+2, r_{BI}{:} r_{BI}+2] \mathrel{+}= K_i[7{:}9,10{:}12]$

        $K[r_{BI}{:}r_{BI}+2, r_{BI}{:} r_{BI}+2] \mathrel{+}= K_i[10{:}12,1{:}3]$

        $K[r_{BI}{:}r_{BI}+2, s_{BI}{:} s_{BI}+2] \mathrel{+}= K_i[10{:}12,4{:}6]$

        $K[r_{BI}{:}r_{BI}+2, t_{BI}{:} t_{BI}+2] \mathrel{+}= K_i[10{:}12,7{:}9]$

        $K[r_{BI}{:}r_{BI}+2, r_{BI}{:} r_{BI}+2] \mathrel{+}= K_i[10{:}12,10{:}12]$

    end for

$$K = \begin{bmatrix}
k^1_{1,1} & k^1_{1,2} & k^1_{1,3} & k^1_{1,4} & k^1_{1,5} & k^1_{1,6} & k^1_{1,7} & k^1_{1,8} & k^1_{1,9} & k^1_{1,10} & k^1_{1,11} & k^1_{1,12} & 0 & 0 & 0 \\
k^1_{2,1} & k^1_{2,2} & k^1_{2,3} & k^1_{2,4} & k^1_{2,5} & k^1_{2,6} & k^1_{2,7} & k^1_{2,8} & k^1_{2,9} & k^1_{2,10} & k^1_{2,11} & k^1_{2,12} & 0 & 0 & 0 \\
k^1_{3,1} & k^1_{3,2} & k^1_{3,3} & k^1_{3,4} & k^1_{3,5} & k^1_{3,6} & k^1_{3,7} & k^1_{3,8} & k^1_{3,9} & k^1_{3,10} & k^1_{3,11} & k^1_{3,12} & 0 & 0 & 0 \\
k^1_{4,1} & k^1_{4,2} & k^1_{4,3} & k^1_{4,4}+k^2_{1,1} & k^1_{4,5}+k^2_{1,2} & k^1_{4,6}+k^2_{1,3} & k^1_{4,7}+k^2_{1,4} & k^1_{4,8}+k^2_{1,5} & k^1_{4,9}+k^2_{1,6} & k^1_{4,10}+k^2_{1,7} & k^1_{4,11}+k^2_{1,8} & k^1_{4,12}+k^2_{1,9} & k^2_{1,10} & k^2_{1,11} & k^2_{1,12} \\
k^1_{5,1} & k^1_{5,2} & k^1_{5,3} & k^1_{5,4}+k^2_{2,1} & k^1_{5,5}+k^2_{2,2} & k^1_{5,6}+k^2_{2,3} & k^1_{5,7}+k^2_{2,4} & k^1_{5,8}+k^2_{2,5} & k^1_{5,9}+k^2_{2,6} & k^1_{5,10}+k^2_{2,7} & k^1_{5,11}+k^2_{2,8} & k^1_{5,12}+k^2_{2,9} & k^2_{2,10} & k^2_{2,11} & k^2_{2,12} \\
k^1_{6,1} & k^1_{6,2} & k^1_{6,3} & k^1_{6,4}+k^2_{3,1} & k^1_{6,5}+k^2_{3,2} & k^1_{6,6}+k^2_{3,3} & k^1_{6,7}+k^2_{3,4} & k^1_{6,8}+k^2_{3,5} & k^1_{6,9}+k^2_{3,6} & k^1_{6,10}+k^2_{3,7} & k^1_{6,11}+k^2_{3,8} & k^1_{6,12}+k^2_{3,9} & k^2_{3,10} & k^2_{3,11} & k^2_{3,12} \\
k^1_{7,1} & k^1_{7,2} & k^1_{7,3} & k^1_{7,4}+k^2_{4,1} & k^1_{7,5}+k^2_{4,2} & k^1_{7,6}+k^2_{4,3} & k^1_{7,7}+k^2_{4,4} & k^1_{7,8}+k^2_{4,5} & k^1_{7,9}+k^2_{4,6} & k^1_{7,10}+k^2_{4,7} & k^1_{7,11}+k^2_{4,8} & k^1_{7,12}+k^2_{4,9} & k^2_{4,10} & k^2_{4,11} & k^2_{4,12} \\
k^1_{8,1} & k^1_{8,2} & k^1_{8,3} & k^1_{8,4}+k^2_{5,1} & k^1_{8,5}+k^2_{5,2} & k^1_{8,6}+k^2_{5,3} & k^1_{8,7}+k^2_{5,4} & k^1_{8,8}+k^2_{5,5} & k^1_{8,9}+k^2_{5,6} & k^1_{8,10}+k^2_{5,7} & k^1_{8,11}+k^2_{5,8} & k^1_{8,12}+k^2_{5,9} & k^2_{5,10} & k^2_{5,11} & k^2_{5,12} \\
k^1_{9,1} & k^1_{9,2} & k^1_{9,3} & k^1_{9,4}+k^2_{6,1} & k^1_{9,5}+k^2_{6,2} & k^1_{9,6}+k^2_{6,3} & k^1_{9,7}+k^2_{6,4} & k^1_{9,8}+k^2_{6,5} & k^1_{9,9}+k^2_{6,6} & k^1_{9,10}+k^2_{6,7} & k^1_{9,11}+k^2_{6,8} & k^1_{9,12}+k^2_{6,9} & k^2_{6,10} & k^2_{6,11} & k^2_{6,12} \\
k^1_{10,1} & k^1_{10,2} & k^1_{10,3} & k^1_{10,4}+k^2_{7,1} & k^1_{10,5}+k^2_{7,2} & k^1_{10,6}+k^2_{7,3} & k^1_{10,7}+k^2_{7,4} & k^1_{10,8}+k^2_{7,5} & k^1_{10,9}+k^2_{7,6} & k^1_{10,10}+k^2_{7,7} & k^1_{10,11}+k^2_{7,8} & k^1_{10,12}+k^2_{7,9} & k^2_{7,10} & k^2_{7,11} & k^2_{7,12} \\
k^1_{11,1} & k^1_{11,2} & k^1_{11,3} & k^1_{11,4}+k^2_{8,1} & k^1_{11,5}+k^2_{8,2} & k^1_{11,6}+k^2_{8,3} & k^1_{11,7}+k^2_{8,4} & k^1_{11,8}+k^2_{8,5} & k^1_{11,9}+k^2_{8,6} & k^1_{11,10}+k^2_{8,7} & k^1_{11,11}+k^2_{8,8} & k^1_{11,12}+k^2_{8,9} & k^2_{8,10} & k^2_{8,11} & k^2_{8,12} \\
k^1_{12,1} & k^1_{12,2} & k^1_{12,3} & k^1_{12,4}+k^2_{9,1} & k^1_{12,5}+k^2_{9,2} & k^1_{12,6}+k^2_{9,3} & k^1_{12,7}+k^2_{9,4} & k^1_{12,8}+k^2_{9,5} & k^1_{12,9}+k^2_{9,6} & k^1_{12,10}+k^2_{9,7} & k^1_{12,11}+k^2_{9,8} & k^1_{12,12}+k^2_{9,9} & k^2_{9,10} & k^2_{9,11} & k^2_{9,12} \\
0 & 0 & 0 & k^2_{10,1} & k^2_{10,2} & k^2_{10,3} & k^2_{10,4} & k^2_{10,5} & k^2_{10,6} & k^2_{10,7} & k^2_{10,8} & k^2_{10,9} & k^2_{10,10} & k^2_{10,11} & k^2_{10,12} \\
0 & 0 & 0 & k^2_{11,1} & k^2_{11,2} & k^2_{11,3} & k^2_{11,4} & k^2_{11,5} & k^2_{11,6} & k^2_{11,7} & k^2_{11,8} & k^2_{11,9} & k^2_{11,10} & k^2_{11,11} & k^2_{11,12} \\
0 & 0 & 0 & k^2_{12,1} & k^2_{12,2} & k^2_{12,3} & k^2_{12,4} & k^2_{12,5} & k^2_{12,6} & k^2_{12,7} & k^2_{12,8} & k^2_{12,9} & k^2_{12,10} & k^2_{12,11} & k^2_{12,12}
\end{bmatrix}. \tag{4.32}$$

4.1.4 Applying Boundary Conditions

After assembling the elemental stiffness matrices and nodal force vectors, boundary conditions are applied by assigning $1s$ and $0s$ to the corresponding rows and columns according to constrained nodes by Algorithm 2.

Algorithm 2 Boundary Value Assignment

---

    for i $= 1$ to BC (BC is the number of constrained nodes) **do**

        BI is $((i^{th}$ constrained node - 1) $\times$ 3) + 1

        K[BI: BI + 2, 1: dimension] = 0

        K[1: dimension, BI: BI + 2] = 0

        K[BI, BI] = 1

        K[BI+1, BI+1] = 1

        K[BI+2, BI+2] = 1

        F[BI: BI + 2] = 0

    end for

The system in Figure 4.3 is constrained from nodes 1, 2, and 3. Algorithm 2 is used to obtain the global stiffness matrix K:

$$
K = \begin{bmatrix}
1 & 0 & 0 & 0 & 0 & 0 & 0 & 0 & 0 & 0 & 0 & 0 & 0 & 0 & 0 \\
0 & 1 & 0 & 0 & 0 & 0 & 0 & 0 & 0 & 0 & 0 & 0 & 0 & 0 & 0 \\
0 & 0 & 1 & 0 & 0 & 0 & 0 & 0 & 0 & 0 & 0 & 0 & 0 & 0 & 0 \\
0 & 0 & 0 & 1 & 0 & 0 & 0 & 0 & 0 & 0 & 0 & 0 & 0 & 0 & 0 \\
0 & 0 & 0 & 0 & 1 & 0 & 0 & 0 & 0 & 0 & 0 & 0 & 0 & 0 & 0 \\
0 & 0 & 0 & 0 & 0 & 1 & 0 & 0 & 0 & 0 & 0 & 0 & 0 & 0 & 0 \\
0 & 0 & 0 & 0 & 0 & 0 & 1 & 0 & 0 & 0 & 0 & 0 & 0 & 0 & 0 \\
0 & 0 & 0 & 0 & 0 & 0 & 0 & 1 & 0 & 0 & 0 & 0 & 0 & 0 & 0 \\
0 & 0 & 0 & 0 & 0 & 0 & 0 & 0 & 1 & 0 & 0 & 0 & 0 & 0 & 0 \\
0 & 0 & 0 & 0 & 0 & 0 & 0 & 0 & 0 & k^1_{10,10}+k^2_{7,7} & k^1_{10,11}+k^2_{7,8} & k^1_{10,12}+k^2_{7,9} & k^2_{7,10} & k^2_{7,11} & k^2_{7,12} \\
0 & 0 & 0 & 0 & 0 & 0 & 0 & 0 & 0 & k^1_{11,10}+k^2_{8,7} & k^1_{11,11}+k^2_{8,8} & k^1_{11,12}+k^2_{8,9} & k^2_{8,10} & k^2_{8,11} & k^2_{8,12} \\
0 & 0 & 0 & 0 & 0 & 0 & 0 & 0 & 0 & k^1_{12,10}+k^2_{9,7} & k^1_{12,11}+k^2_{9,8} & k^1_{12,12}+k^2_{9,9} & k^2_{9,10} & k^2_{9,11} & k^2_{9,12} \\
0 & 0 & 0 & 0 & 0 & 0 & 0 & 0 & 0 & k^2_{10,7} & k^2_{10,8} & k^2_{10,9} & k^2_{10,10} & k^2_{10,11} & k^2_{10,12} \\
0 & 0 & 0 & 0 & 0 & 0 & 0 & 0 & 0 & k^2_{11,7} & k^2_{11,8} & k^2_{11,9} & k^2_{11,10} & k^2_{11,11} & k^2_{11,12} \\
0 & 0 & 0 & 0 & 0 & 0 & 0 & 0 & 0 & k^2_{12,7} & k^2_{12,8} & k^2_{12,9} & k^2_{12,10} & k^2_{12,11} & k^2_{12,12}
\end{bmatrix}.
$$

$$(4.33)$$

4.1.5 Solution of the Linear System

After applying boundary conditions to the elemental stiffness matrices and nodal force vectors, the whole system is one large linear system:

$$Ku = f. \tag{4.34}$$

In the last step, solving the system gives unknown nodal displacements

$$u = K^{-1}f. \tag{4.35}$$

Chapter 5

Non-Linear Finite Element Method

This chapter explains in detail the stages of the nonlinear FEM and a verification procedure for measuring the correctness of the proposed nonlinear FEM.

5.1 Non-Linear FEM using Tetrahedral Elements with Green-Lagrange Strains

Proposed system uses non-linear FEM due to accuracy reasons. In this chapter, algorithm of non-linear FEM solution, the development of Green-Lagrange strains (large deformation strains) η that leads to non-linear FEM, stiffness matrix K and the solution of the system with Newton-Raphson method will be explained. Our proposed non-linear FEM solution algorithm for 3D tetrahedral element consist of 4 main parts:

1. Tetrahedralization;

2. Construction of nonlinear elemental stiffness matrices;

3. Construction of nonlinear element residuals;

4. Solution of the non-linear system with Newton-Raphson method that gives unknown nodal displacements.

The proposed nonlinear FEM uses linear FEM's style in the sense that it does not require the explicit use of weight functions, differential equations and integrals. Moreover, our approach extends the linear FEM to the nonlinear FEM by extending the linear strains to the Green-Lagrange strains.

5.1.1 Tetrahedralization

We have the information of nodal positions and which nodes belong to which element from the tetrahedralization process like we did for linear FEM solution. We use nodal positions to construct elemental stiffness matrices, and element's nodal information to assemble the element's Jacobian matrices to form global Jacobian matrices and element's residuals to form global residual vectors for every step of Newton-Raphson process.

5.1.2 Construction of Nonlinear Elemental Stiffness Matrices

The displacements are represented with linear shape functions, as in linear FEM. The calculation of the parameters α, β, γ, δ, V (the volume of tetrahedron), and the shape functions are the same as it is done in linear FEM.

Nonlinear FEM differs from linear FEM because of the nonlinearity that arises from the higher order term neglected in Equation 4.16. The strain vector that is used in linear FEM relies on the assumption that the displacements at x, y and z axes are very small. The initial and final positions of a given particle are practically the same; thus, the higher terms are neglected [**?**]. When the displacements are large, however, this is no longer the case and one must distinguish between

the initial and final coordinates of particles, so the higher order terms are added into the strain equations.

$$(A'B')^2 = \left(dx + \frac{\partial u_x}{\partial x}dx\right)^2 + \left(\frac{\partial u_y}{\partial x}dx\right)^2. \tag{5.1}$$

By adding the higher order terms, 3D strains are defined as [?]:

$$
\begin{aligned}
\eta_{xx} &= \frac{\partial u_x}{\partial x} + \frac{1}{2}\left[\left(\frac{\partial u_x}{\partial x}\frac{\partial u_x}{\partial x}\right) + \left(\frac{\partial u_y}{\partial x}\frac{\partial u_y}{\partial x}\right) + \left(\frac{\partial u_z}{\partial x}\frac{\partial u_z}{\partial x}\right)\right] \\[2mm]
\eta_{yy} &= \frac{\partial u_y}{\partial y} + \frac{1}{2}\left[\left(\frac{\partial u_x}{\partial y}\frac{\partial u_x}{\partial y}\right) + \left(\frac{\partial u_y}{\partial y}\frac{\partial u_y}{\partial y}\right) + \left(\frac{\partial u_z}{\partial y}\frac{\partial u_z}{\partial y}\right)\right] \\[2mm]
\eta_{zz} &= \frac{\partial u_z}{\partial z} + \frac{1}{2}\left[\left(\frac{\partial u_x}{\partial z}\frac{\partial u_x}{\partial z}\right) + \left(\frac{\partial u_y}{\partial z}\frac{\partial u_y}{\partial z}\right) + \left(\frac{\partial u_z}{\partial z}\frac{\partial u_z}{\partial z}\right)\right] \\[2mm]
\gamma_{xy} &= \frac{1}{2}\left(\frac{\partial u_x}{\partial y} + \frac{\partial u_y}{\partial x}\right) + \frac{1}{2}\left[\left(\frac{\partial u_x}{\partial x}\frac{\partial u_x}{\partial y}\right) + \left(\frac{\partial u_y}{\partial x}\frac{\partial u_y}{\partial y}\right) + \left(\frac{\partial u_z}{\partial x}\frac{\partial u_z}{\partial y}\right)\right] \\[2mm]
\gamma_{zx} &= \frac{1}{2}\left(\frac{\partial u_z}{\partial x} + \frac{\partial u_x}{\partial z}\right) + \frac{1}{2}\left[\left(\frac{\partial u_x}{\partial z}\frac{\partial u_x}{\partial x}\right) + \left(\frac{\partial u_y}{\partial z}\frac{\partial u_y}{\partial x}\right) + \left(\frac{\partial u_z}{\partial z}\frac{\partial u_z}{\partial x}\right)\right] \\[2mm]
\gamma_{yz} &= \frac{1}{2}\left(\frac{\partial u_y}{\partial z} + \frac{\partial u_z}{\partial y}\right) + \frac{1}{2}\left[\left(\frac{\partial u_x}{\partial y}\frac{\partial u_x}{\partial z}\right) + \left(\frac{\partial u_y}{\partial y}\frac{\partial u_y}{\partial z}\right) + \left(\frac{\partial u_z}{\partial y}\frac{\partial u_z}{\partial z}\right)\right]
\end{aligned}
\tag{5.2}
$$

that leads to

$$\{\eta\} = \begin{Bmatrix} \eta_{xx} \\ \eta_{yy} \\ \eta_{zz} \\ 2\left(\gamma_{xy} + \gamma_{yx}\right) \\ 2\left(\gamma_{xz} + \gamma_{zx}\right) \\ 2\left(\gamma_{yz} + \gamma_{zy}\right) \end{Bmatrix} = \begin{Bmatrix} \eta_{xx} \\ \eta_{yy} \\ \eta_{zz} \\ 2\eta_{xy} \\ 2\eta_{zx} \\ 2\eta_{yz} \end{Bmatrix}. \tag{5.3}$$

Green-Lagrange strain tensor is represented in matrix notation as

$${\eta} = [B_L]{d} + \frac{1}{2}{d}^T[B_{NL}]{d}, \tag{5.4}$$

where ${d}$ is the nodal displacements, $[B_L]$ is the linear and $[B_{NL}]$ is the nonlinear part of the $[B_0]$ matrix [?]. For a specific element, $[B_L]$ and $[B_{NL}]$ are constant, as the $[B]$ matrix in linear FEM. With the modification of ${d}$ by introducing secant and tangent relations [?], Equation 5.4 becomes

$$\begin{aligned}
{\eta} &= \left([B_L] + \tfrac{1}{2}{d^T}[B_{NL}]\right){d} = [B_0]{d}, \\
{\bar{\eta}} &= \left([B_L] + {d^T}[B_{NL}]\right){d} = [\bar{B}_0]{d}.
\end{aligned} \tag{5.5}$$

The linear part of the $[B_0]$ matrix ($[B_L]$) is same as the $[B]$ matrix in linear FEM. The calculation of $[B_0]$ becomes more complex with the introduction of the nonlinear terms. After finding the nonlinear strains, these equations are combined with the shape functions to find matrix $[B_0]$

$${\bar{\eta}} = [\bar{B}_0]{d}. \tag{5.6}$$

The most frequently used terms for the calculation of the nonlinear strains are $\frac{\partial u_x}{\partial x}$, $\frac{\partial u_x}{\partial y}$, $\frac{\partial u_x}{\partial z}$, $\frac{\partial u_y}{\partial x}$, $\frac{\partial u_y}{\partial y}$, $\frac{\partial u_y}{\partial x}$, $\frac{\partial u_z}{\partial x}$, $\frac{\partial u_z}{\partial y}$ and $\frac{\partial u_z}{\partial z}$. They are represented by

$$\begin{aligned}
u_{xx} &= (\beta_1 u_1 + \beta_2 u_2 + \beta_3 u_3 + \beta_4 u_4) \\
u_{yx} &= (\beta_1 v_1 + \beta_2 v_2 + \beta_3 v_3 + \beta_4 v_4) \\
u_{zx} &= (\beta_1 w_1 + \beta_2 w_2 + \beta_3 w_3 + \beta_4 w_4) \\
u_{xy} &= (\gamma_1 u_1 + \gamma_2 u_2 + \gamma_3 u_3 + \gamma_4 u_4) \\
u_{yy} &= (\gamma_1 v_1 + \gamma_2 v_2 + \gamma_3 v_3 + \gamma_4 v_4) \\
u_{zy} &= (\gamma_1 w_1 + \gamma_2 w_2 + \gamma_3 w_3 + \gamma_4 w_4) \\
u_{xz} &= (\delta_1 u_1 + \delta_2 u_2 + \delta_3 u_3 + \delta_4 u_4) \\
u_{yz} &= (\delta_1 v_1 + \delta_2 v_2 + \delta_3 v_3 + \delta_4 v_4) \\
u_{zz} &= (\delta_1 w_1 + \delta_2 w_2 + \delta_3 w_3 + \delta_4 w_4)
\end{aligned} \tag{5.7}$$

where u_{xx} represents $\frac{\partial u_x}{\partial x}$.

Using the linear parts of Equation 4.13 for displacements, we can evaluate the partial derivatives of the shape functions as follows (for the 1st node of $[B_{NL}]$):

$$\left[\left(\frac{\partial u_x}{\partial x}\frac{\partial u_x}{\partial x}\right) + \left(\frac{\partial u_y}{\partial x}\frac{\partial u_y}{\partial x}\right) + \left(\frac{\partial u_z}{\partial x}\frac{\partial u_z}{\partial x}\right)\right] = \frac{1}{6V}\left(\beta_1(u_{xx} + u_{yx} + u_{zx})\right)$$

$$\left[\left(\frac{\partial u_x}{\partial y}\frac{\partial u_x}{\partial y}\right) + \left(\frac{\partial u_y}{\partial y}\frac{\partial u_y}{\partial y}\right) + \left(\frac{\partial u_z}{\partial y}\frac{\partial u_z}{\partial y}\right)\right] = \frac{1}{6V}\left(\gamma_1(u_{xy} + u_{yy} + u_{zy})\right)$$

$$\left[\left(\frac{\partial u_x}{\partial z}\frac{\partial u_x}{\partial z}\right) + \left(\frac{\partial u_y}{\partial z}\frac{\partial u_y}{\partial z}\right) + \left(\frac{\partial u_z}{\partial z}\frac{\partial u_z}{\partial z}\right)\right] = \frac{1}{6V}\left(\delta_1(u_{xz} + u_{yz} + u_{zz})\right)$$

$$\left[\left(\frac{\partial u_x}{\partial x}\frac{\partial u_x}{\partial y}\right) + \left(\frac{\partial u_y}{\partial x}\frac{\partial u_y}{\partial y}\right) + \left(\frac{\partial u_z}{\partial x}\frac{\partial u_z}{\partial y}\right)\right] = \frac{1}{6V}\left(\gamma_1(u_{xx} + u_{yx} + u_{zx})\right)+$$
$$\frac{1}{6V}\left(\beta_1(u_{xy} + u_{yy} + u_{zy})\right)$$

$$\left[\left(\frac{\partial u_x}{\partial z}\frac{\partial u_x}{\partial x}\right) + \left(\frac{\partial u_y}{\partial z}\frac{\partial u_y}{\partial x}\right) + \left(\frac{\partial u_z}{\partial z}\frac{\partial u_z}{\partial x}\right)\right] = \frac{1}{6V}\left(\delta_1(u_{xx} + u_{yx} + u_{zx})\right)+$$
$$\frac{1}{6V}\left(\beta_1(u_{xz} + u_{yz} + u_{zz})\right)$$

$$\left[\left(\frac{\partial u_x}{\partial y}\frac{\partial u_x}{\partial z}\right) + \left(\frac{\partial u_y}{\partial y}\frac{\partial u_y}{\partial z}\right) + \left(\frac{\partial u_z}{\partial y}\frac{\partial u_z}{\partial z}\right)\right] = \frac{1}{6V}\left(\gamma_1(u_{xz} + u_{yz} + u_{zz})\right)+$$
$$\frac{1}{6V}\left(\delta_1(u_{xy} + u_{yy} + u_{zy})\right)$$

(5.8)

Using Equations 5.5 and 5.8, we obtain $[\bar{B}_0]$ for the 1st node

$$[\bar{B}_{0_1}] = \begin{bmatrix} \beta_1 + \beta_1(u_{xx}) & \beta_1(u_{yx}) & \beta_1(u_{zx}) \\ \gamma_1(u_{xy}) & \gamma_1 + \gamma_1(u_{yy}) & \gamma_1(u_{zy}) \\ \delta_1(u_{xz}) & \delta_1(u_{yz}) & \delta_1 + \delta_1(u_{zz}) \\ \gamma_1 + \gamma_1(u_{xx}) + \beta_1(u_{xy}) & \gamma_1(u_{yx}) + \beta_1 + \beta_1(u_{yy}) & \gamma_1(u_{zx}) + \beta_1(u_{zy}) \\ \delta_1 + \delta_1(u_{xx}) + \beta_1(u_{xz}) & \delta_1(u_{yx}) + \beta_1(u_{yz}) & \delta_1(u_{zx}) + \beta_1 + \beta_1(u_{zz}) \\ \gamma_1(u_{xz}) + \delta_1(u_{xy}) & \gamma_1 + \gamma_1(u_{yz}) + \delta_1(u_{yy}) & \gamma_1(u_{zz}) + \delta_1 + \delta_1(u_{zy}) \end{bmatrix} \begin{Bmatrix} u_1 \\ v_1 \\ w_1 \end{Bmatrix} .$$

(5.9)

Similarly, using Equations 5.5 and 5.8, we obtain $[B_0]$ for the 1st node

$$[B_{0_1}] =$$

$$
\begin{bmatrix}
\beta_1 + \frac{1}{2}\beta_1(u_{xx}) & \frac{1}{2}\beta_1(u_{yx}) & \frac{1}{2}\beta_1(u_{zx}) \\
\frac{1}{2}\gamma_1(u_{xy}) & \gamma_1 + \frac{1}{2}\gamma_1(u_{yy}) & \frac{1}{2}\gamma_1(u_{zy}) \\
\frac{1}{2}\delta_1(u_{xz}) & \frac{1}{2}\delta_1(u_{yz}) & \delta_1 + \frac{1}{2}\delta_1(u_{zz}) \\
\gamma_1 + \frac{1}{2}\gamma_1(u_{xx}) + \frac{1}{2}\beta_1(u_{xy}) & \frac{1}{2}\gamma_1(u_{yx}) + \beta_1 + \frac{1}{2}\beta_1(u_{yy}) & \frac{1}{2}\gamma_1(u_{zx}) + \frac{1}{2}\beta_1(u_{zy}) \\
\delta_1 + \frac{1}{2}\delta_1(u_{xx}) + \frac{1}{2}\beta_1(u_{xz}) & \frac{1}{2}\delta_1(u_{yx}) + \frac{1}{2}\beta_1(u_{yz}) & \frac{1}{2}\delta_1(u_{zx}) + \beta_1 + \frac{1}{2}\beta_1(u_{zz}) \\
\frac{1}{2}\gamma_1(u_{xz}) + \frac{1}{2}\delta_1(u_{xy}) & \gamma_1 + \frac{1}{2}\gamma_1(u_{yz}) + \frac{1}{2}\delta_1(u_{yy}) & \frac{1}{2}\gamma_1(u_{zz}) + \delta_1 + \frac{1}{2}\delta_1(u_{zy})
\end{bmatrix}
\begin{Bmatrix} u_1 \\ v_1 \\ w_1 \end{Bmatrix}.
$$

$$(5.10)$$

From Equation 2.3, the engineering stress vector τ is related to the strain vector by

$$\tau = [E]\{\bar{\eta}\} = [E][\bar{B}_0]\{d\}. \tag{5.11}$$

From the conservation of the potential energy, substituting Equations 5.4 and 5.11 into Equation 2.3, we obtain the element stiffness matrix

$$[k(u)] = \int \int \int \{d\}^T [B_0]^T [E][\bar{B}_0]\{d\} dx\, dy\, dz. \tag{5.12}$$

We can discard the integrals as we did for linear FEM. $[B_0]$, $[E]$ and $[\bar{B}_0]$ are constant for tetrahedral element, so that Equation 5.12 is rewritten by

$$[k(u)] = \{d\}^T [B_0]^T [E][\bar{B}_0]\{d\} V. \tag{5.13}$$

Introducing nodal forces, we obtain

$$\{f\} = \begin{Bmatrix} f_{1x} \\ f_{1y} \\ f_{1z} \\ \vdots \\ f_{4x} \\ f_{4y} \\ f_{4z} \end{Bmatrix} \{d\}^T. \tag{5.14}$$

With the equilibrium equation, and the cancellation of the $\{d\}^T$ the whole system for one element reduces to

$$k(d)^e \{d\}^e = f^e. \tag{5.15}$$

By substituting $\{d\}$ by u, we obtain

$$k(u)^e u^e = f^e. \tag{5.16}$$

Finally, there are only nonlinear displacement functions left, which are solved with the Newton-Raphson method to find the unknown displacements u.

5.1.3   Construction of Nonlinear Element Residuals

Element residuals are necessary for the iterative Newton-Raphson method. The element residual is a 12×1 vector for a specific element. The residual for a specific element is defined as

$$r^e = k(u)^e - f^e. \tag{5.17}$$

Having determined r^e, we can now express Equation 5.17 in expanded vector form as

$$
\begin{Bmatrix} r_1 \\ r_2 \\ r_3 \\ \vdots \\ r_{12} \end{Bmatrix} = \begin{bmatrix} k(u)_{(1,1)} + k(u)_{(1,2)} + k(u)_{(1,3)} + \ldots + k(u)_{(1,12)} \\ k(u)_{(2,1)} + k(u)_{(2,2)} + k(u)_{(2,3)} + \ldots + k(u)_{(2,12)} \\ k(u)_{(3,1)} + k(u)_{(3,2)} + k(u)_{(3,3)} + \ldots + k(u)_{(3,12)} \\ \vdots \\ k(u)_{(12,1)} + k(u)_{(12,2)} + k(u)_{(12,3)} + \ldots + k(u)_{(12,12)} \end{bmatrix} - \begin{Bmatrix} f_1 \\ f_2 \\ f_3 \\ \vdots \\ f_{12} \end{Bmatrix}.
$$
(5.18)

The tangent stiffness matrix $[K]_T^e$ (r'^e) is also necessary for the iterative Newton-Raphson method. The tangent stiffness matrix is also 12×12 matrix, like the elemental stiffness matrix. However, the tangent stiffness matrix depends on residuals, unlike the elemental stiffness matrix. Elemental stiffness matrices are used to construct residuals and the derivatives of the residuals are used to construct the elemental tangent stiffness matrices. We can express the elemental tangent stiffness matrix for a specific element as

$$
r'^e = [K]_T^e = \begin{bmatrix} \frac{\partial}{\partial u_1} r_1 & \frac{\partial}{\partial v_1} r_1 & \frac{\partial}{\partial w_1} r_1 & \cdots & \frac{\partial}{\partial u_4} r_1 & \frac{\partial}{\partial v_4} r_1 & \frac{\partial}{\partial w_4} r_1 \\ \frac{\partial}{\partial u_1} r_2 & \frac{\partial}{\partial v_1} r_2 & \frac{\partial}{\partial w_1} r_2 & \cdots & \frac{\partial}{\partial u_4} r_2 & \frac{\partial}{\partial v_4} r_2 & \frac{\partial}{\partial w_4} r_2 \\ \frac{\partial}{\partial u_1} r_3 & \frac{\partial}{\partial v_1} r_3 & \frac{\partial}{\partial w_1} r_3 & \cdots & \frac{\partial}{\partial u_4} r_3 & \frac{\partial}{\partial v_4} r_3 & \frac{\partial}{\partial w_4} r_3 \\ \vdots & \vdots & \vdots & \vdots & \vdots & \vdots & \vdots \\ \frac{\partial}{\partial u_1} r_{12} & \frac{\partial}{\partial v_1} r_{12} & \frac{\partial}{\partial w_1} r_{12} & \cdots & \frac{\partial}{\partial u_4} r_{12} & \frac{\partial}{\partial v_4} r_{12} & \frac{\partial}{\partial w_4} r_{12} \end{bmatrix}.
$$
(5.19)

5.1.4 Solution of the Non-linear System with Newton-Raphson Method

Newton-Raphson method is a fast and popular numerical method for solving non-linear equations [**?**], as compared to the other methods, such as direct iteration. In principle, the method works by applying two steps (cf. Algorithm 3): (i) check if the equilibrium is reached within the desired accuracy; (ii) if not, make a suitable adjustment to the state of the deformation [**?**]. An initial guess for displacements are needed to start the iterations. The displacements are updated according to

$$x_{k+1} = x_k - \frac{f_{x_k}}{f'_{x_k}}. \tag{5.20}$$

Algorithm 3 Newton-Raphson method

Make initial guess $f(x)$
while $|f(x)| \leq \delta$ **do**
    Compute $p = -\frac{f(x)}{f'(x)}$
    Update $x = x + p$
    Calculate $f(x)$
end while

In our nonlinear solution, u is the vector that keeps the information of the nodal displacements. Instead of making only one assumption, we make whole u vector initial guess in order to start the iteration.

$$u_1 = u_0 - \frac{r_{u_0}}{r'_{u_0}}, \tag{5.21}$$

where r is residual of the global stiffness matrix $[K]$ calculated in Equation 5.18 and r' is the tangent stiffness matrix calculated in Equation 5.19.

At every step, the vector r and the matrix r' are updated for every element with the new u_i values. Then, r and r' are assembled as we did with for the global stiffness matrix K and the global force vector F in linear FEM. Boundary conditions are applied to the global r vector and the global r' matrix. Using the global r vector and the global r' matrix, we have

$$
\begin{aligned}
r'(u_i)p &= -r(u_i), \quad \text{and} \\
p &= -(r'(u_i))^{-1}r(u_i).
\end{aligned}
\tag{5.22}
$$

u_i is updated with the solution of Equation 5.22.

$$u_{i+1} = u_i + p. \tag{5.23}$$

Then, we check if the equilibrium is reached within the desired accuracy defined by δ as

$$|r(u_i)| \leq \delta. \tag{5.24}$$

After the desired accuracy is reached, the unknown nodal displacements are found.

5.2 Verification of the Proposed Approach

Verification is one of the important steps of the finite element analysis. We verified our approach with Pedersen's analytical stiffness matrices for tetrahedral elements solution [**?**]. In the experiments we obtained the same displacement amount with his method. In this section, Pedersen's method is explained in order to see the differences between our approach and his approach.

Both approaches give the same results since they use the same Green-Lagrange strains and tetrahedral elements. However, the computation times differ because of different methods to calculate the stiffness matrices. Pedersen divides the elemental stiffness matrices S into nine sub-matrices, $[S_{xx}]$, $[S_{xy}]$, $[S_{xz}]$, $[S_{yx}]$, $[S_{yy}]$, $[S_{yz}]$, $[S_{zx}]$, $[S_{zy}]$ and $[S_{zz}]$, which is represented as K (12×12 stiffness matrix) in our method.

$$S[1:4, 1:4] = [S_{xx}]$$
$$S[1:4, 5:8] = [S_{xy}]$$
$$S[1:4, 9:12] = [S_{xz}]$$
$$S[5:8, 1:4] = [S_{yx}]$$
$$S[5:8, 5:8] = [S_{yy}] \qquad (5.25)$$
$$S[5:8, 9:12] = [S_{yz}]$$
$$S[9:12, 1:4] = [S_{zx}]$$
$$S[9:12, 5:8] = [S_{zy}]$$
$$S[9:12, 9:12] = [S_{zz}]$$

These nine sub-matrices are calculated with 81 linear combination factors. Pedersen obtains $[S]_{xx}$ as

$$
\begin{aligned}
[S]_{xx} =\ & A_{xxxx}[T_{xx}] + A_{xxyy}[T_{yy}] + A_{xxzz}[T_{zz}] + A_{xxxy}[T_{xy}] + A_{xxyx}[T^T_{xy}] + \\
& A_{xxxz}[T_{xz}] + A_{xxzx}[T^T_{xz}] + A_{xxyz}[T_{yz}] + A_{xxzy}[T^T_{yz}] \qquad (5.26)
\end{aligned}
$$

$[T]$ sub-matrices coincide with the linear part of our global stiffness matrix $[K]$. In other words, the matrix $[T_{xx}]$ is obtained by

$$
[T_{xx}] =
\begin{bmatrix}
q_x^2 & -p_{5968}q_x & -p_{3829}q_x & -p_{2635}q_x \\
-p_{5968}q_x & p_{5968}^2 & p_{5968}p_{3829} & p_{5968}p_{2635} \\
-p_{3829}q_x & p_{5968}p_{3829} & p_{23829} & p_{3829}p_{2635} \\
-p_{2635}q_x & p_{5968}p_{2635} & p_{3829}p_{2635} & p_{2635}^2
\end{bmatrix}
\qquad (5.27)
$$

following the short notation defined by Pedersen, e.g., $p_{5968} = p_5 p_9 - p_6 p_8$. When we expand the unknown term, q_x, in Equation 5.27, it becomes $-\beta_1$ in our method:

$$
\begin{aligned}
q_x &= p_{5968} + p_{3829} + p_{2635} \\
q_x &= (y_3 z_4 - y_4 z_3) + (z_2 y_4 - z_4 y_2) + (y_2 z_3 - y_3 z_2) \\
\beta_1 &= -y_3 z_4 + y_4 z_3 - z_2 y_4 + z_4 y_2 - y_2 z_3 + y_3 z_2 \\
q_x &= -\beta_1
\end{aligned}
\qquad (5.28)
$$

As it is seen from Equation 5.29, the other terms that Pedersen used are the same as the ones used in our method.

$$
\begin{aligned}
q_x &= -\beta_1 \\
p_{5968} &= \beta_2 \\
p_{3829} &= \beta_3 \\
p_{2635} &= \beta_4 \\
q_y &= -\gamma_1 \\
p_{6749} &= \gamma_2 \\
p_{1937} &= \gamma_3 \\
p_{3416} &= \gamma_4 \\
q_z &= \delta_1 \\
p_{4857} &= \delta_2 \\
p_{2718} &= \delta_3 \\
p_{1524} &= \delta_4
\end{aligned}
\tag{5.29}
$$

Apart from the stiffness matrix calculation, the solutions of the nonlinear equations in both methods are the same. Both approaches use the Newton-Raphson method to find the unknown displacements. Hence, the comparison of the computation time required to calculate the stiffness matrices is sufficient to compare the performances of two approaches.

Chapter 6

Experimental Results

We conducted eight experiments to compare the linear and nonlinear finite element methods. Moreover, we compared the proposed nonlinear FEM method with the Pedersen's method [**?**].

First, we present how we construct FEM models and continue with error analysis for linear and nonlinear FEM solution with the cube mesh. We make analysis with increasing the mesh's density and comparing the displacements for a selected node.

In the first experiment, our aim is to observe the strain-displacement relationship. The test model is a cube with six elements. We also examine the force-displacement relationship for a selected node to compare the displacements for linear and nonlinear FEMs.

The rest of the experiments are performed with different test models. Our aim in these experiments is to compare the accuracy of the deformations for linear and nonlinear FEMs. The results for these experiments are interpreted by comparing displacement amounts for the force applied nodes and all the nodes. Finally, the computational costs of different methods are compared, including experiments on single-core and multi-cores to assess the parallelization of the methods.

6.1 Construction of the FEM Models

The construction of the FEM models consists of three stages:

1. Reading surface meshes. The meshes for the cube, beam and the cross surface models are constructed manually, and the liver mesh is taken from 3D Mesh Research Database [**?**].

2. Tetrahedralization of the surface mesh using TetGen [**?**]. We also improve the quality of the models using TetGen.

3. Interactive specification of the constrained (fixed) nodes and the nodes to which the forces to be applied.

6.2 Load Steps

Multiple load steps are used when the load forces are time-dependent or simulation is dynamic [**?**]. Our simulation is static not time dependent so we used single load step in all of our experiments.

6.3 Material Properties

We used linear material properties for the models in the experiments. We used 1 for Young's modulus (ϵ), and 0.25 for Poisson's ratio (ν).

6.4 Error Analysis

The error analysis is one of the crucial steps of the finite element method to assess the quality of the computed results. We need to make error analysis using approximate results when the exact solution is not available. The error analysis

Element	Displacement - z	Element	Displacement - z	Error (%)
6	0.3831	48	0.3995	4.105
48	0.3995	384	0.4027	0.794
384	0.4027	1536	0.4025	0.049

Table 6.1: Element displacements (in centimeters) along the z-axis for node 4 and their corresponding error ratios for linear FEM

is performed by comparing the displacements of the two approximate results by increasing the number of elements in meshes uniformly. We choose a cube mesh of size 10cm^3 to work with because uniformly increasing the number of elements of the cube is much easier than using a complex mesh.

□

Figure 6.1: The cube mesh with six elements (left) and 48 elements (right).

$$\| u^d - u^{\frac{d}{2}} \| = C \| (u - u^{\frac{d}{2}}) \| \qquad (6.1)$$

The error analysis is achieved by comparing the displacements with mesh density d and $\frac{d}{2}$ in 1D (Equation 6.1). If we adapt the 1D formula to 3D, we need to increase the density by 8-times (for every dimension by d to $\frac{d}{2}$) for error analysis. Figure 6.1 shows that number of elements are increased from 6 to 48 for the first step.

The force amount must be the same for each step to observe the displacement errors. Hence, the cube is constrained from the bottom face and pulled towards the direction of the black arrow with same amount of force uniformly distributed among the green nodes (4 units for both the 6- and 48-element meshes) for each step. We choose the node that is highlighted by red arrow to observe the displacements. Moreover, we limited our analysis with 1536 elements because of the high computational cost of nonlinear FEM.

The results in Table 6.1 and 6.2 show that the difference $u^d - u^{\frac{d}{8}}$ decreases with mesh refinement in each step. Using Equation 2.8, we can state that the solutions of the linear and nonlinear FEM are valid and converges.

Element	Displacement - z	Element	Displacement - z	Error (%)
6	0.3622	48	0.3795	4.558
48	0.3795	384	0.3751	1.159
384	0.375162	1536	0.375101	0.016

Table 6.2: Element displacements (in centimeters) along the z-axis for node 4 and their corresponding error ratios for nonlinear FEM

□

Figure 6.2: Linear FEM error analysis with *L2* and *Energy* norms

The error norms are required to compute the error for the whole solution. *L2* and *Energy* norms are the most frequently used norms to compute the errors. They are defined as

$$L_2 = \sqrt{\int \int \int e^2 \, dx \, dy \, dz} \ \text{ and}$$

$$Energy = \sqrt{\frac{1}{2} \int \int \int \frac{\partial e}{\partial x} + \frac{\partial e}{\partial y} + \frac{\partial e}{\partial z} \, dx \, dy \, dz,} \tag{6.2}$$

where e is the error. The error is computed by subtracting the actual solution u for mesh density d from the approximate solution u_N for mesh density $\frac{d}{2}$. Figures 6.2 and 6.3 show that the error decreases linearly and converges with mesh refinement in each step.

□

Figure 6.3: Nonlinear FEM error analysis with *L2* and *Energy* norms

6.5   Experiment 1

The first experiment is conducted with a cube mesh that has eight nodes and six tetrahedral elements. Figure 6.4 shows that the cube is constrained from the upper four nodes and pulled downwards with a small amount of force (one unit force for each of the upper four nodes). This experiment is conducted with such a small mesh in order to examine the nodal displacements and strains for each element explicitly. Tables 6.3 and 6.4 show force displacements at node 4 using the linear and nonlinear FEMs, respectively. Figures 6.5 and 6.6 show the initial and final positions of the nodes for the linear and nonlinear FEMs, respectively. As it is seen in Figures 6.5 and 6.6, the linear and nonlinear methods produce similar displacements when the force magnitude is small. Table 6.5 gives a comparison of the 1st element strain for the linear and nonlinear FEMs. Table 6.5 shows that even the force magnitude is small, there are differences in strains that can affect displacements. Figure 6.8 shows that the displacement increases linearly with the force magnitude. However, nonlinear FEM behaves exponentially as expected due to the nonlinear strain definitions. Figure 6.7 depicts the convergence of the Newton-Raphson method for the nonlinear FEM.

□

Figure 6.4: Experiment 1: A cube mesh of size 10 cm^3 with eight nodes and six tetrahedra is constrained from the blue nodes and is pulled downwards from the green nodes.

Node	Displacement - x	Displacement - y	Displacement - z
1	0.027234	0.011064	-0.289965
2	0.004306	-0.109719	-0.440739
3	-0.066065	-0.056547	-0.343519
4	-0.107536	0.070143	-0.514524
5	0	0	0
6	0	0	0
7	0	0	0
8	0	0	0

Table 6.3: Force displacements (in centimeters) at node 4 using linear FEM.

□

Figure 6.5: The initial and final positions of the nodes for the linear FEM. The red spheres show the initial positions and the green spheres show the final positions of the nodes.

Node	Displacement - x	Displacement - y	Displacement - z
1	0.029911	0.012665	-0.278365
2	0.008606	-0.103350	-0.415594
3	-0.058835	-0.051901	-0.324126
4	-0.098945	0.068928	-0.478495
5	0	0	0
6	0	0	0
7	0	0	0
8	0	0	0

Table 6.4: The displacements (in centimeters) of the nodes using the nonlinear FEM.

□

Figure 6.6: The initial and final positions of the nodes for the nonlinear FEM. The red spheres show the initial positions and the green spheres show the final positions of the nodes.

	Linear FEM	Nonlinear FEM	Error (%)
s_{xx}	0	0	-
s_{yy}	0	0	-
s_{zz}	0.0290	0.0282	-2.76
s_{xy}	0	0	-
s_{xz}	-0.0027	-0.0030	11.11
s_{yz}	-0.0011	-0.0013	18.18

Table 6.5: Comparison of the 1st element strain. The error represents the linear FEM's strain error according to the nonlinear FEM's strain.

□

Figure 6.7: Newton-Raphson convergence graphics for the nonlinear FEM.

□

Figure 6.8: Force displacements (in centimeters) at node 4 for the linear and nonlinear FEMs.

6.6 Experiment 2

The second experiment is conducted with a cube but with 82 nodes and 224-tetrahedral elements. Figure 6.9 shows that the cube is constrained from the bottom face and pulled upwards with a small amount of force (one unit force for each of the lower four nodes). This experiment is conducted with more tetrahedral elements in order to examine the displacement differences and the shape of the mesh after applying two methods.As it is seen from Figures 6.10 and 6.11, the linear and nonlinear methods produce similar displacements because small and large strains provide similar displacements when the force magnitude is small. Therefore, the overall nodal displacement error becomes 0.65%. However, the difference between the results of two methods can be seen from the upper part of the cube; the displacement at the upper face of the cube with linear FEM is more compared to the nonlinear FEM. It can be observed that the force applied nodes (green nodes) produce 5.45% of the error. Moreover, the shape of the cube is more distorted with linear FEM; the left and the right sides of the cube are bent more in linear FEM; the shape of the cube is preserved better with nonlinear FEM.

□

Figure 6.9: Experiment 2: A cube mesh of size 10 cm^3 with 82 nodes and 224-tetrahedra is constrained from blue nodes and is pulled along the arrow from green nodes.

□

Figure 6.10: The final shape of the mesh for the linear FEM (top left: wireframe tetrahedral mesh; top right: wireframe tetrahedral mesh with nodes; bottom left: wireframe surface mesh; bottom right: shaded mesh)

□

Figure 6.11: The final shape of the mesh for the nonlinear FEM (top left: wireframe tetrahedral mesh; upper right: wireframe tetrahedralmesh with nodes; lower left: wireframe surface mesh; lower right: shaded mesh)

6.7   Experiment 3

The third experiment is conducted with the beam that has 90 nodes and 216-tetrahedral elements. Figures 6.12 (a) and (b) show that the beam is constrained from the blue nodes, and twisted from the both ends of the beam. This experiment is conducted to observe different effects of the nonlinear and the linear FEM deformations on the beam. In the twist experiment, the differences can be seen better. Figures 6.13 and 6.14 show that the nodes that generate the edges of the beam differ (shown with arrow) from each other. In Figure 6.13, the nodes are straight, which is not the desired result of the twist operation. This is the result of usage of linear strains so that linear FEM produced straight displacement. However, at Figure 6.14 nodes are curvy, which is is the expected result of the twist operation. Overall nodal displacement error is 3.10% due to the curvy twist of the nonlinear FEM. It can be observed from the force applied nodes(green nodes), force applied nodes produces 9.61% of error, in linear FEM general shape of the face that hosts the force applied nodes, is more distorted than the nonlinear FEM.

□
(a)

□
(b)

Figure 6.12: Experiment 3: The beam mesh is constrained from the blue nodes and twisted from the green nodes. (a) Front view; (b) Side view, which also shows the force directions applied on each green node.

□

Figure 6.13: Linear FEM solution (top left: wireframe tetrahedra and nodes; top right: only nodes; bottom left: wireframe surface mesh; lower right: shaded mesh).

□

Figure 6.14: Nonlinear FEM solution (top left: wireframe tetrahedra and nodes; top right: only nodes; bottom left: wireframe surface mesh; lower right: shaded mesh).

6.8   Experiment 4

The fourth experiment is conducted with the same beam (Section 6.7) that has 90 nodes and 216-tetrahedral elements. Figure 6.15 shows that the beam is constrained from the blue nodes, and pushed downwards at the green nodes. This experiment is conducted to observe different effects of the nonlinear and the linear FEM deformations over the beam mesh. It can be observed that with linear FEM, the beam is bent more than with nonlinear FEM. The width of the beam become wider with the linear FEM at the both ends (see Figure 6.16). On the other hand, the deformation is smoother with nonlinear FEM (see Figure 6.17). This volume difference results in overall 4.32% error among all nodes, and 15.95% error on force applied nodes (green nodes).

□

Figure 6.15: Experiment 4: The beam mesh is constrained from the blue nodes and pushed downwards at the green nodes.

□

Figure 6.16: Linear FEM solution (top: wireframe tetrahedra and nodes; middle upper: shaded mesh; middle lower: initial mesh and the final tetrahedra are overlaid; bottom: initial and final meshes are overlaid).

□

Figure 6.17: Nonlinear FEM solution (top: wireframe tetrahedra and nodes; middle upper: shaded mesh; middle lower: initial mesh and the final tetrahedra are overlaid; bottom: initial and final meshes are overlaid).

6.9   Experiment 5

This experiment is conducted with the cross mesh that has 159 nodes and 244-tetrahedral elements. Figure 6.18 shows that the cross-shape is constrained from the blue nodes and pushed towards the green nodes. This experiment is conducted to observe the different effects of nonlinear and linear FEM deformations over the cross-shaped mesh with high amount of force (50 units). It can be observed that under a high amount of force, linear FEM produces unexpected result by expanding the upper and the lower part of the mesh (cf. Figures 6.19 and 6.20). As a result of that, the overall nodal displacement and force node displacement errors are 213.36% and 232.56%, respectively. It can be said that under a high amount of force, nonlinear FEM produces accurate, thus more realistic, results (cf. Figures 6.21 and 6.22).

□

Figure 6.18: Experiment 5: The cross mesh is constrained from the blue nodes and pushed towards the green nodes.

□
(a)

□
(b)

Figure 6.19: Linear FEM solution: (a) wireframe mesh; (b) shaded mesh.

□
(a)

□
(b)

Figure 6.20: Linear FEM solution: (a) initial and final wireframe meshes are overlaid; (b) initial and final shaded meshes are overlaid.

□
(a)

□
(b)

Figure 6.21: Nonlinear FEM solution: (a) wireframe mesh; (b) shaded mesh.

□
(a)

□
(b)

Figure 6.22: Nonlinear FEM solution: (a) initial and final wireframe meshes are overlaid; (b) initial and final shaded meshes are overlaid.

6.10 Experiment 6

The sixth experiment is conducted with the liver mesh [**?**] that has 465 nodes and 1560-tetrahedral elements. Figure 6.23 shows that the liver mesh is constrained from the blue nodes, and pulled from the green nodes towards the arrow direction. This experiment is conducted to observe the different effects of the nonlinear and the linear FEM deformations over the liver. Linear FEM produces a protrusion at the top of the mesh (see Figure 6.24). It can be observed that the liver mesh is deformed more realistically and smoothly with nonlinear FEM (see Figure 6.25). As a result of the protrusion generated for the linear FEM, the node displacement error becomes 12.85%. Apart from the force-applied region, the overall shape is preserved (the overall nodal displacement error is 0.72%) in both methods due to the low amount of force. We can conclude that with dense meshes, nonlinear FEM produces accurate, thus more realistic, results.

□

Figure 6.23: Experiment 6: The liver mesh is constrained from the blue nodes and pulled from the green nodes (left: initial nodes; right: initial shaded mesh and nodes).

□
(a)

□
(b)

□
(c)

Figure 6.24: Linear FEM solution: (a) left: nodes, right: tetrahedral wireframe mesh; (b) left: wireframe surface mesh, right: wireframe surface mesh with nodes; (c) left: shaded mesh, right: shaded mesh with nodes.

☐
(a)

☐
(b)

☐
(c)

Figure 6.25: Nonlinear FEM solution: (a) left: nodes, right: tetrahedral wireframe mesh; (b) left: wireframe surface mesh, right: wireframe surface mesh with nodes; (c) left: shaded mesh, right: shaded mesh with nodes.

6.11   Experiment 7

This experiment is conducted with the liver mesh that has 465 nodes and 1560-tetrahedral elements. Figure 6.26 shows that the liver mesh is constrained from the blue nodes, and pulled from the green node towards the arrow direction. This experiment is conducted to observe the different effects of the nonlinear and the linear FEM deformations over the liver with pulling only one node. It can be observed that the linear FEM produces a high amount of displacement around the force node (see Figure 6.27). As a result of that, the node displacement error becomes 58.94%. The liver mesh is deformed more realistically and smoothly with nonlinear FEM (see Figure 6.28). Apart from the force-applied region, the overall shape is preserved (the overall nodal displacement error is 0.12%). It can be said that with dense meshes, nonlinear FEM produces accurate, thus more realistic, results.

□

Figure 6.26: Experiment 7: The liver mesh is constrained from the blue nodes and pulled from the green node (left: initial nodes, right: initial shaded mesh and nodes).

□
(a)

□
(b)

□
(c)

Figure 6.27: Linear FEM solution: (a) left: nodes, right: tetrahedral wireframe mesh; (b) left: wireframe surface mesh, right: wireframe surface mesh with nodes; (c) left: shaded mesh, right: shaded mesh with nodes.

□
(a)

□
(b)

□
(c)

Figure 6.28: Nonlinear FEM solution: (a) left: nodes, right: tetrahedral wireframe mesh; (b) left: wireframe surface mesh, right: wireframe surface mesh with nodes; (c) left: shaded mesh, right: shaded mesh with nodes.

6.12   Experiment 8

This experiment is again conducted with the liver mesh that has 465 nodes and 1560-tetrahedral elements. Figure 6.29 shows that the liver mesh is constrained from the blue nodes, and pushed upwards at the green nodes. This experiment is conducted to observe the different effects of the nonlinear and the linear FEM deformations over the liver when pushing the liver from several nodes. Linear FEM produced high amount of displacement around the force node (see Figure 6.30). As a result of that, the node displacement error becomes 17.28%. It can be observed that the liver mesh is deformed more realistically and smoothly with nonlinear FEM (see Figure 6.31). The mesh is more collapsed inwards with linear FEM, whereas its structure is better preserved with nonlinear FEM. Apart from the force applied region, the overall shape is preserved (the overall nodal displacement error is 0.1%).

□

Figure 6.29: Experiment 8: The liver mesh is constrained from the blue nodes and pushed towards the green nodes (left - initial nodes, right - initial shaded mesh and nodes).

□
(a)

□
(b)

Figure 6.30: Linear FEM solution: (a) left: nodes, right: shaded mesh with nodes; (b) the mesh from a different view, left: shaded mesh with nodes, right: shaded mesh.

□
(a)

□
(b)

Figure 6.31: Nonlinear FEM solution: (a) left: nodes, right: shaded mesh with nodes; (b) the mesh from a different view, left: shaded mesh with nodes, right: shaded mesh.

6.13   Computational Cost Analysis

The computation times of the finite element experiments are required to make comparison of how much our proposed solution is faster than Pedersen's solution. Moreover, we can observe that nonlinear FEM has higher computation cost than linear FEM. However, high computation cost gives us much more accurate results that we can ignore this high cost when we are working with crucial simulations like car crash tests, surgical simulators (in terms of accuracy) and concrete analysis of the building.

When comparing nonlinear solutions, we calculated the computation times of construction of the stiffness matrices and the whole solution in order to state how different calculation of stiffness matrices directly affects the stiffness matrices' and the whole solution's computation time. Moreover, we conducted these experiments on two different systems to analyze how clock speed of the processor affects the computation time and to state the multi-core efficiencies on different systems. We conducted all the experiments on a desktop computer with Core i7 processor overclocked at $4.0GHz$ with 24GB of RAM. Table 6.6, Figures 6.32 and 6.36 show the computation times required to calculate the stiffness matrix. Table 6.7, Figures 6.34 and 6.38 show the computation times required to solve the system.

Figures 6.33, 6.35, 6.37, 6.39 and 6.40 depict the speed-ups of each experiment obtained by using the proposed approach with respect to the Pedersen's method for different number of cores and threads. The speed-up is calculated by

$$\text{Speed-up} = \frac{\text{Runtime(Pedersen's method)}}{\text{Runtime(The proposed approach)}} \tag{6.3}$$

Figure 6.41 shows the speed-up of multi-core over the single-core on our system. Multicore efficiency obtained using a multi-core with respect to a single core is given by

$$\text{Multicore Efficiency} = \left(\frac{\text{Runtime(Single-core)}}{\text{Runtime(Multi-core)}} \right) \times 100 \qquad (6.4)$$

We used Matlab's Parallel Computing Toolbox to implement multithreading. The toolbox provides local workers (Matlab computational engines) that distributes the program into threads to execute applications on a multicore system [?]. We implemented multithreading by using *parfor* loop instead of *for* loop. When iterating over the elements to calculate stiffness matrices, residuals and tangent stiffness matrices, part of the computation is stayed on main Matlab worker, and the rest of the parts are computed on local workers. When *parfor* loop starts, necessary data is sent from the main thread to local workers, and at the end of the *parfor* loop, the results are sent back to the main thread and combined together.

The proposed solution is highly parallelizable; our program works 3.6 times faster when it is distributed on 4-core. Overhead of creating local workers is relatively high when number of elements is small. In this case, multi threaded solution becomes less efficient than the single threaded solution (cf. Figure 6.41).

The proposed method outperforms the Pedersen's method. On the average, it is 111% faster at computing stiffness matrices since Pedersen's method uses much more symbolic terms (cf. Figure 6.40). However, both methods uses Newton-Raphson method to solve nonlinear equations which takes 90% of the computation time. Therefore overall speed-up decreases to 16% on average (cf. Figure 6.40).

□

Figure 6.32: Comparison of the computation times required to calculate the stiffness matrix (single thread).

□

Figure 6.33: Relative performance comparison of the stiffness matrix calculation (single thread).

□

Figure 6.34: Comparison of the computation times required to solve the system (single thread).

Experiment	Linear	Pedersen	Pedersen MT	Prop Non	Prop Non MT
1st - 6	0.0572	0.8341	1.8073	0.3783	0.6109
2nd - 224	0.1753	38.3624	8.4493	19.8544	3.8807
3rd - 226	0.1692	32.5297	8.0717	15.3335	3.7179
4th - 216	0.1699	34.1291	8.0912	16.2847	3.7356
5th - 244	0.1861	36.9055	8.5068	18.2106	4.0998
6th - 1560	0.9178	266.3396	65.1570	125.6929	36.7951
7th - 1560	0.8851	265.0623	65.9921	124.0710	37.0265
8th - 1560	0.9979	266.4710	65.4512	124.4716	37.1006

Table 6.6: Computation times (in seconds) of the stiffness matrices for all experiments (MT: Multi thread, Prop Non: The proposed nonlinear solution).

□

Figure 6.35: Relative performance comparison of the system solution (single thread).

Experiment	Linear	Pedersen	Pedersen MT	Prop Non	Prop Non MT
1st - 6	0.0592	4.8396	3.4315	4.3774	2.1489
2nd - 224	0.2359	402.0249	94.9423	341.0334	79.4478
3rd - 226	0.2274	460.6526	128.5903	394.5419	103.0223
4th - 216	0.2282	459.8582	125.2817	448.9026	122.0369
5th - 244	0.2557	2267.3736	656.7743	1967.2491	513.2731
6th - 1560	1.4029	4492.5631	909.9521	3574.6976	865.8751
7th - 1560	1.3644	5736.3210	1274.7842	4636.2668	1224.7844
8th - 1560	1.3878	4849.1274	1004.8713	3926.7512	972.4567

Table 6.7: Computation times (in seconds) of the systems for all experiments. (MT: Multi thread, Prop Non: The proposed nonlinear solution).

□

Figure 6.36: Comparison of the computation times required to calculate the stiffness matrix (eight threads on four cores).

□

Figure 6.37: Relative performance comparison of the stiffness matrix calculation (eight threads on four cores).

□

Figure 6.38: Comparison of the computation times required to solve the system (eight threads on four cores).

□

Figure 6.39: Relative performance comparison of the system solution (eight threads on four cores).

□

Figure 6.40: Relative performance comparison averaged over all experiments.

□

Figure 6.41: Multi-core efficiency of the proposed approach (speed-up of eight threads on four cores over the single core).

Chapter 7

Conclusion and Future Work

We have presented a new non-linear FEM solution method. The proposed solution is easier to analyze in terms of constructing the elemental stiffness matrices and faster than Pedersen's solution. The proposed solution is approximately twice faster on the average at computing stiffness matrices and 17% faster at computing the whole system than the Pedersen's solution.

We compared our solution with linear FEM to see advantages and drawbacks in eight different experiments. Our proposed solution has huge advantages over the linear FEM in terms of accuracy. The proposed solution handles large deformations and small deformations perfectly although difference in small deformations is low. However, this low amount of difference cannot be neglected for applications that require very high accuracy. Parallelization is also important to speed-up the FEM solution. We obtain significant speed-ups on multicore machines.

Although the proposed solution has significant advantages over linear FEM and recent non-linear solution, there is still room for development. Possible future extensions are as follows:

1. Although Newton-Raphson is a fast solution technique, over 90% of the computation time of the whole system spent in Newton-Raphson solution

procedure. It can be implemented better to overcome jumping to the un-expected roots or different solution procedure can be implemented.

2. The proposed solution is highly parallelizable so it can benefit from a GPU implementation. However, the nonlinear solution procedure uses over 6GB of system memory when computing the solution for over 1500 elements, so we need GPUs that has lots of memory.

3. Although we decreased the system memory usage by simplifying the solution procedure for the nonlinear solution, it uses a significant amount of system memory. Hence, the solution procedure can be optimized more to decrease the memory usage.

4. All experiments are conducted with the same material properties. They can be extended by measuring the exact properties of the real objects (i.e., an actual liver).

Bibliography

[1] M. Müller, B. Heidelberger, M. Hennix, and J. Ratcliff. Position based dynamics. *J. Vis. Comun. Image Represent.*, 18(2):109–118, Apr. 2007.

Appendix A

Rhinoplasty Application

We conducted two different experiments to apply our solution in the area of rhinoplasty. In the experiments, we correct the form of misshapen noses (see Figure A.1). We compare the accuracy of the deformations for linear and nonlinear FEMs. The results for these experiments are interpreted by comparing displacement amounts for the force applied nodes and all the nodes.

A.1   Experiment 1

The first experiment is conducted with a head mesh that has 6709 nodes and 25722 tetrahedral elements (see Figure A.2 (a)). Number of tetrahedral elements are very high. However, all the operations are done in the nose area with 1458 tetrahedral elements. To simplify the calculations, stationary tetrahedral elements are not taken into account. Figure A.2 (b) shows that the head mesh is constrained from the blue nodes, and is pushed upwards at the green nodes. This experiment is conducted to observe the different effects of the nonlinear and the linear FEM deformations over the nose. Linear FEM produced high amount of displacement at the upper part of the nose (see Figure A.2 (c)). As a result of that, the node displacement error becomes 64.92%. It can be observed that the

□

Figure A.1: The perfect nose.

nose was deformed more realistically and smoothly with nonlinear FEM (see Figure A.2 (d)). The nose is more collapsed inwards with linear FEM, whereas its structure is better preserved with nonlinear FEM and the overall shape is more similar to a perfect nose than linear FEM. Although, nearly 6000 nodes are constrained, the overall nodal displacement error is 3.88%.

□ □

(a)   (b)

□ □

(c)   (d)

Figure A.2: Experiment 1: (a) Initial misshapen nose. (b) Head mesh is constrained from the blue nodes, and is pushed upwards at the green nodes. (c) Linear FEM Solution: left: wireframe surface mesh with nodes, right: shaded mesh with texture. (d) Nonlinear FEM Solution: left: wireframe surface mesh with nodes, right: shaded mesh with texture.

A.2   Experiment 2

The second experiment is conducted with mesh similar to the one used in the first experiment. However, it has 7071 nodes and 27020 tetrahedral elements due to different shape of the nose and tetrahedralization (see Figure A.3 (a)). To simplify the calculations, stationary tetrahedral elements are not taken into account. 4511 tetrahedra are included in the calculations. A.3 (b) shows that the head mesh is constrained from the blue nodes, and is pushed upwards at the green nodes. This experiment is conducted to observe the different effects of the nonlinear and the linear FEM deformations over the nose. Linear FEM produced high amount of displacement at the lower part of the nose (see A.3 (c)). Moreover, the nose is nearly collapsed inwards that is far away from the perfect nose. As a result of that, the node displacement error becomes 96.03%. With nonlinear FEM, the nose is deformed more realistically and smoothly (see A.3 (d)). The nose is more collapsed inwards with linear FEM, whereas its structure is better preserved with nonlinear FEM and the overall shape is more similar to a perfect nose than linear FEM. Although, nearly 5000 nodes are constrained, the overall nodal displacement error is 11.19%.

(a)   (b)

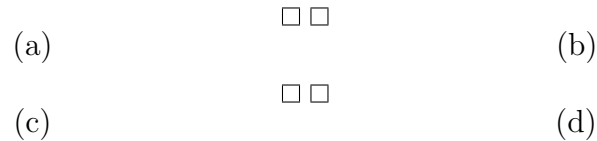(c)   (d)

Figure A.3: Experiment 2: (a) Initial misshapen nose. (b) Head mesh is constrained from the blue nodes, and is pushed upwards at the green nodes. (c) Linear FEM Solution: left: wireframe surface mesh with nodes, right: shaded mesh with texture. (d) Nonlinear FEM Solution: left: wireframe surface mesh with nodes, right: shaded mesh with texture.